Clearance Pathways and Tumor Targeting of Imaging Nanoparticles

Mengxiao Yu and Jie Zheng*

Department of Chemistry, The University of Texas at Dallas, 800 West Campbell Road, Richardson, Texas 75080, United States

ABSTRACT A basic understanding of how imaging nanoparticles are removed from the normal organs/tissues but retained in the tumors is important for their future clinical applications in early cancer diagnosis and therapy. In this review, we discuss current understandings of clearance pathways and tumor targeting of small-molecule- and inorganic-nanoparticle-based imaging probes with an emphasis on molecular nanoprobes, a class of inorganic nanoprobes that can escape reticuloendothelial system (RES) uptake and be rapidly eliminated from the normal tissues/organs *via* kidneys but can still passively target the tumor with high efficiency through the enhanced permeability permeability and retention (EPR) effect. The impact of nanoparticle design (size, shape, and surface chemistry) on their excretion, pharmacokinetics, and passive tumor targeting were quantitatively discussed. Synergetic integration of effective renal clearance and EPR effect offers a promising pathway to design low-toxicity and high-contrast-enhancement imaging nanoparticles that could meet with the clinical translational requirements of regulatory agencies.

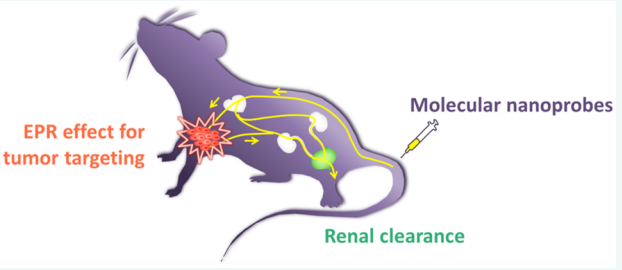

KEYWORDS: imaging nanoparticles · cancer diagnosis · enhanced permeability and retention (EPR) effect · molecular nanoprobes · reticuloendothelial system (RES) · renal clearance · tumor targeting · clinical translation

Imaging techniques, allowing visualization of structural and functional changes inside the body, are being widely used in clinical cancer diagnosis.[1,2] While computed tomography (CT) and magnetic resonance imaging (MRI) can detect tumor upon the endogenous difference between cancerous and normal tissues, both spatial and temporal resolutions for tumor imaging are severely limited by many common features shared by cancer and surrounding normal tissues, particularly on the early stage of cancer development. Thus, exogenous chemical agents that can enhance the contrast between cancerous and normal tissues are highly desired for early cancer diagnosis, a key to improving survival rates and life quality of cancer patients. Owing to the development of various types of contrast agents, high-resolution and high-contrast cancer imaging has been extended to both low-cost fluorescence technique in preclinical studies and the highly sensitive radiological modalities in clinical practice such as positron emission tomography (PET) and single-photon emission computed tomography (SPECT).

To meet the requirements of U.S. Food and Drug Administration (FDA), all injected contrast agents need to be cleared from the body completely in a reasonable time period.[3] Thus, the most common contrast agents used in clinical practice are small-molecule-based (namely molecular probes). While molecular probes designed for different imaging modalities exhibit diversity in chemical structures, properties, and functionalities, they often share some similar behaviors *in vivo*: after being intravenously (iv) injected, they rapidly distribute into various organs (short distribution half-life), circulate in the body with a short blood elimination half-life, and most of them are eventually excreted through the urinary system in a short-time period (Figure 1A). Such two-compartment pharmacokinetics and efficient renal clearance not only allow rapid tumor targeting, but also minimize the potential hazards to normal tissues and healthy organs. However, it is challenging to integrate either multiple modalities or therapy into one molecule, which has been driving continuous development of new generations of contrast agents to advance early cancer diagnosis.

* Address correspondence to jiezheng@utdallas.edu.

Received for review March 1, 2015 and accepted July 6, 2015.

Published online July 06, 2015
10.1021/acsnano.5b01320

Inorganic nanoparticles (NPs)-based contrast agents (namely nanoprobes) with assistance of quantum size effect, often show strong signal output and multifunctionalities that small molecules generally do not possess,[4,5] holding great promise to shift current medical paradigm to early detection and therapy. For example, quantum dots (QDs) with bright, robust and tunable fluorescence have been used for highly sensitive tumor diagnosis.[5−7] Magnetic iron oxide NPs can further enhance MRI contrast and allow magnetic field directed drug delivery.[8−10] Gold NPs can effectively convert light energy into heat and serve as agents for photothermal therapy.[11,12] In addition, by taking advantage of the unique tumor structure (hypervasculature, defective vascular architecture, and impaired lymphatic drainage), NPs can often selectively accumulate in the primary and metastatic tumor sites at much higher concentrations for longer times than small molecular probes, with no need of active targeting ligands (Figure 1B). However, unlike small molecular probes, inorganic NPs are often rapidly sequestered from the blood and severely accumulate in reticuloendothelial system (RES) organs (liver, spleen, *etc.*). While the severe and rapid RES uptake of inorganic NPs has been reduced and slowed down by surface coating with poly(ethylene glycol) (PEG) molecules,[13] a majority of PEGylated NPs still end up in the liver and spleen after circulation, resulting in low tumor targeting specificity (defined as tumor-to-liver ratio for nonrenal clearabe NPs) and potential long-term toxicity.

Since both nanoprobes and small molecular probes have unique strengths in cancer imaging, integration of these strengths into a single probe is expected to lead to significant improvements in clinically translatable nanomedicines for early cancer diagnosis and therapy. A list of these properties include:

(1) Size-dependent properties;
(2) Multimodality;
(3) Strong EPR effect;
(4) Long-term circulation in blood (prolonged elimination half-life);
(5) High physiological stability;
(6) Efficient renal clearance;
(7) Minimum accumulation in nontargeted tissues and organs;
(8) Rapid distribution to various organs and tissues (short distribution half-life);
(9) Low perturbation on the labeled biomolecules (binding affinity, cellular dynamics, *etc.*).

Most inorganic NPs can meet the first four criteria, whereas most small molecules can carry the next five properties. A new generation of renal clearable inorganic NPs has been engineered to meet these nine requirements. Like small molecular probes, the renal clearable inorganic NPs show rapid whole body distribution, efficient renal clearance, and low accumulation in RES organs. On the other hand, they behave like conventional NPs and can exhibit prolonged blood circulation, selectively distribute in the tumor sites at high concentration, and accumulate in tumor through EPR effect. These renal clearable inorganic NPs, carrying the strengths of both nonrenal clearable NPs and small molecules in cancer imaging, are named "molecular nanoprobes" (Figure 1C). Herein, we will give a brief review on molecular nanoprobes by quantitatively comparing them with small molecular probes and conventional nanoprobes in excretion route, pharmacokinetics, and passive tumor targeting *via* EPR effect.

VOCABULARY: Imaging nanoparticles - In this review, we focus on inorganic nanoparticles with different imaging modalities that have potential applications in cancer diagnosis; **Enhanced permeability and retention (EPR) effect** - nanoparticles can passively accumulate in the tumor sites at a high concentration for a long period of time due to the high-density and leaky vascular structure and impaired lymphatic drainage of the solid tumor; **Molecular nanoprobes** - a type of inorganic nanoparticles that can rapidly distribute in the whole body and be eliminated from normal tissues and healthy organs through the urinary system like small molecules while retaining EPR effect in tumor targeting; **Reticuloendothelial system (RES)** - a part of the immune system that primarily comprises phagocytic cells located in the liver, spleen, and other reticular connective tissues and functions to identify and remove foreign substances; **Renal clearance** - an elimination pathway through renal system;

EXCRETION PATHWAY

Excretion is an essential biological process that prevents damage and toxicity by eliminating unwanted materials from the body. There are two major excretion routes: the renal (urine) and hepatic (bile to feces) pathways for contrast agents. In general, renal excretion is preferred because the contrast agents can be rapidly eliminated while little cellular internalization/metabolism is involved, thus effectively minimizing body exposure to the contrast agents. The renal pathway relies on glomerular filtration in the kidneys; thus, the material size, charge, and shape all affect the filtration efficiency. The filtration-size threshold of glomerular capillary walls is typically 6−8 nm for spherical particles (size-, charge-, and surface ligand-dependent within this range),[14] indicating renal excretion is exclusive only for materials with ultrasmall hydrodynamic diameters (HDs).

Excretion Pathway of Small Molecular Probes. Most small molecular probes are small enough to pass the glomerular capillary walls and enter into urine in intact form if they have no interactions with serum proteins during circulation. During the first 24 h after intravenous (iv) injection, renal clearance efficiency of >50% injected dose (% ID) is widely observed in FDA-approved small molecular probes, such as gadolinium chelates for MRI

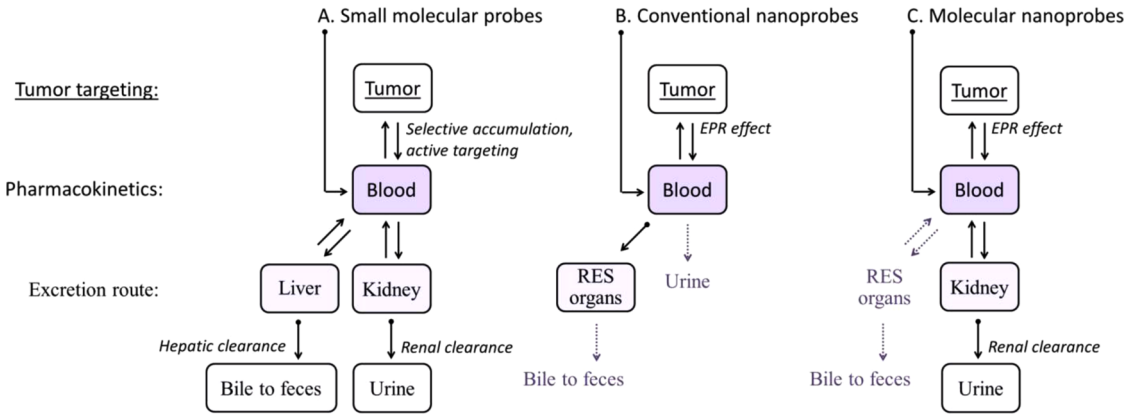

Figure 1. Small molecule-based, conventional nanoparticle-based, and molecular nanoparticle-based cancer imaging probes exhibit different behaviors *in vivo* following intravenous administration. (A) Small molecular probes rapidly distribute into various organs, circulate in the body with a short blood elimination half-life, and are eventually excreted from the body through renal and/or hepatic routes (within several hours or days). The fraction ratio between renal and hepatic excretion varies depending on the nature of the molecules. The tumor uptake of small molecules is generally low; however, small molecular probes with selective tumor accumulation (*e.g.*, [^{18}F]FDG) or conjugation of active targeting ligands (*e.g.*, [^{18}F]-labeled peptides) can show excellent tumor uptake and contrast. (B) Conventional nanoprobes can selectively accumulate and be retained in the tumor sites through EPR effect, but they are severely trapped in the RES organs (liver, spleen, *etc.*) for months to years or are slowly excreted into bile and feces through hepatic route (weeks to months). Since extravasation of nanoparticles from tumor vasculature to extracellular tumor microenvironment could be treated as an accumulative process, the EPR effect of nanoparticles is highly dependent on their pharmacokinetics: high blood concentration, long blood distribution and elimination half-lives, and large area under curve (AUC) are favorable for enhancing the EPR effect and improving tumor targeting efficiency. (C) By integrating the advantages of small molecules and conventional nanoparticles, molecular nanoparticles exhibit efficient clearance from the body through renal route (within several days), low accumulation in RES organs, passive tumor targeting *via* EPR effect, and favorable two-compartment pharmacokinetics for enhancing tumor targeting efficiency. Synergistic integration of the EPR effect with active targeting strategy and environmentally responsive properties can lead to developing next generation of molecular nanoprobes.

(gadodiamide,[15] gadopentetate dimeglumine,[15] and gadoteridol[16]), iodinated contrast agents for CT (iohexol,[17] iopamidol,[17] and iopromide[17]), and ^{99m}Tc complexes for SPECT (^{99m}Tc-iron-ascorbate,[18] ^{99m}Tc-glucoheptonate,[18] and ^{99m}Tc-MAG3[19]) (Figure 2 and Supporting Information Table S1). For clinical cancer diagnosis with PET imaging, [^{18}F]fluoroglucose ([^{18}F]FDG) is the most commonly used contrast agent and urinary excretion of [^{18}F]FDG is ~15% ID in 1.5 h postinjection (h p.i.).[20] In the case of near-infrared fluorophores for *in vivo* fluorescence imaging used in preclinical cancer research, 44.0% ID of IRDye 800 CW and 86.0% ID of ZW800-1 were cleared from the body into urine by 4 h p.i.[21] Because of such rapid and efficient urinary clearance, these small molecular probes after 4 h p.i. generally have low nonspecific accumulation in the vital organs such as kidney (the major organ involved in renal excretion), liver, and spleen (Supporting Information Table S2). Only 0.3% ID of gadodiamide[15] and 0.19% injected dose per gram of tissue (% ID/g) of IRDye 800 CW[22] accumulated in the liver at 24 h p.i. The liver uptakes of ^{64}Cu-DOTA,[23] [^{18}F]FDG[24], and ZW800-1[21] were 0.33, 1.18, and 0.9% ID/g at 46, 12, 4 h p.i., respectively; their kidney uptakes were 0.35, 1.81, and 9.8% ID/g, respectively.

Besides renal clearance, some small molecule probes with enhanced hydrophobicity are eliminated from the body through hepatic route (liver metabolism, bile excretion and feces elimination are involved) because of serum protein binding. After iv administration of ^{99m}Tc-pertechnetate, a SPECT contrast agent, 25−30% ID is excreted in urine in 24 h; following 48−72 h, hepatic excretion is predominant and results in 35% ID in feces. Nearly 40% ID of ^{99m}Tc-pertechnetate was still retained in the body 72 h p.i. and the whole-body clearance half-life is 53 h.[25] Since the average retention time of hepatically excreted contrast agents is much longer than that of renal clearable ones, resulting in increasing health risk, probes with efficient urinary excretion are still preferred in the clinics.

Excretion Pathway of Conventional Nonrenal Clearable Nanoprobes. In contrast to small molecules that can be almost completely eliminated in urine and/or feces within several hours or days, the conventional nanoprobes are often severely trapped in the RES for a long time. Regardless of size, shape, chemical composition and surface coating, the liver accumulation of nonrenal clearable inorganic NPs are generally in the range of 10−100% ID/g at 4−48 h p.i. (Figure 3A), 10−1000 times higher than liver uptake of small molecular probes (0.1−1% ID/g) (Supporting Information Table S2). The conventional nanoprobes generally show HDs above the kidney filtration threshold (6−8 nm) in physiological environment, thus excluding the possibility of renal excretion unless they can dissociate into small fragments. One reason for their large HDs is the large core sizes of the NPs: spherical Au NPs (10−500 nm),[54] Au nanorods (diameter of 10−20 nm

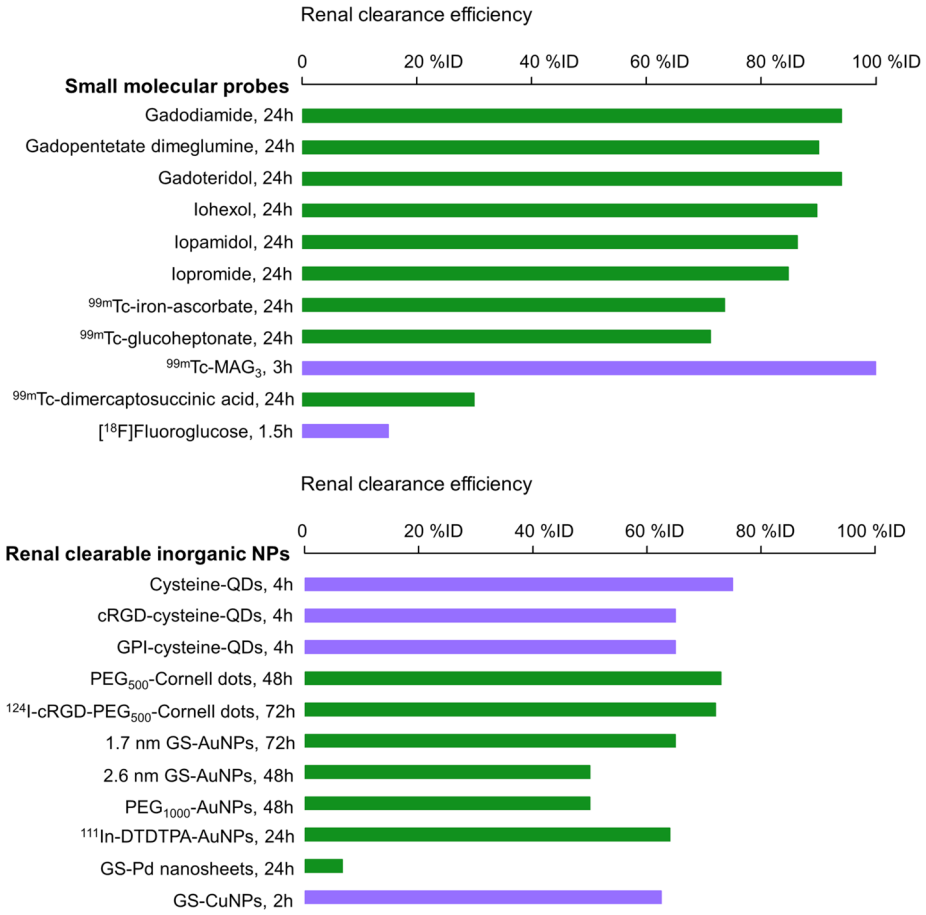

Figure 2. Renal clearance efficiencies of representative clinically used small molecular probes and recently developed renal clearable inorganic nanoparticles (NPs) following intravenous administration. Data values and detailed information about the small molecular probes and renal clearable inorganic NPs are listed in Supporting Information Table S1 and Table 1, respectively. The data measured at 24−72 h p.i. and 1.5−4 h p.i. are respectively marked in green and purple.

and length of 30−100 nm),[55] Au nanocages (30−60 nm),[56] iron oxide NPs (10−90 nm),[57] lanthanide-doped upconversion NPs (20−60 nm),[58,59] solid and mesoporous silica NPs (20−200 nm).[60,61] Another reason is the dramatic increase of HDs due to surface coating, aggregation and serum protein adsorption of NPs in biological fluid, even though some inorganic NPs are ultrasmall in core size (<6 nm). For instance, the core size of Ag_2S QDs is 5.4 nm, but HDs increase to 26.8 nm after coating the surface with six-armed PEG.[32] The HD of PEG_{2000}-capped 5 nm QDs (InAs/InP/ZnSe, core/shell/shell) is 16−18 nm.[36,37] While the core size of lanthanide-doped upconversion NPs ($NaYF_4$: Yb, Er, ^{153}Sm) can be decreased from 20−40 nm to as small as 5 nm, HD of the NPs with PEG_{600} coating is ~9 nm and still larger than the kidney filtration threshold.[62] The adsorption of serum proteins to the QDs (dihydrolipoic acid-coated or cysteamine-coated surface) results in an increase in HD > 15 nm.[3] In addition to increasing the HDs, adsorption of opsonins on NPs (known as "opsonization") also initiates the rapid recognition by the receptors on the cell surface of macrophages in RES (such as Kupffer cells in the liver) and subsequent internalization by macrophages.[63,64] For instance, mercaptoundecanoic acid-coated $CdSe_{0.25}Te_{0.75}$/CdS NIR QDs were rapidly sequestered by the liver and spleen and no QDs were detected in the blood at 3 h p.i.[65] To reduce opsonization, the most common strategy is to conjugate the PEG polymer to the particle surface.[13] Although PEGylation can slow down RES uptake of NPs and prolong the blood circulation time, RES organs are still the dominant accumulation sites for PEG-coated NPs. As shown in Figure 3A, there is no significant difference in the liver uptake between the PEGylated NPs (34.1 ± 21.8% ID/g, $N = 29$) and non-PEGylated NPs (28.1 ± 15.3% ID/g, $N = 12$) ($p > 0.05$) 24 h p. i.

Since Au NPs and protected-QDs are chemically stable and hard to be digested by enzymes in the lysosomes of macrophages, they are often retained in the body for months to years once they are internalized by the macrophages.[66,67] For example, 24 h after iv injection of 40 nm citrate-coated Au NPs, TEM analysis showed that the AuNPs accumulated in almost all the Kupffer cells in the liver and located in lysosome/endosome-like vesicles; only a 9% decrease in Au amount in liver was detected during the following 6 months (by ICP-MS).[68] According to a pilot study in

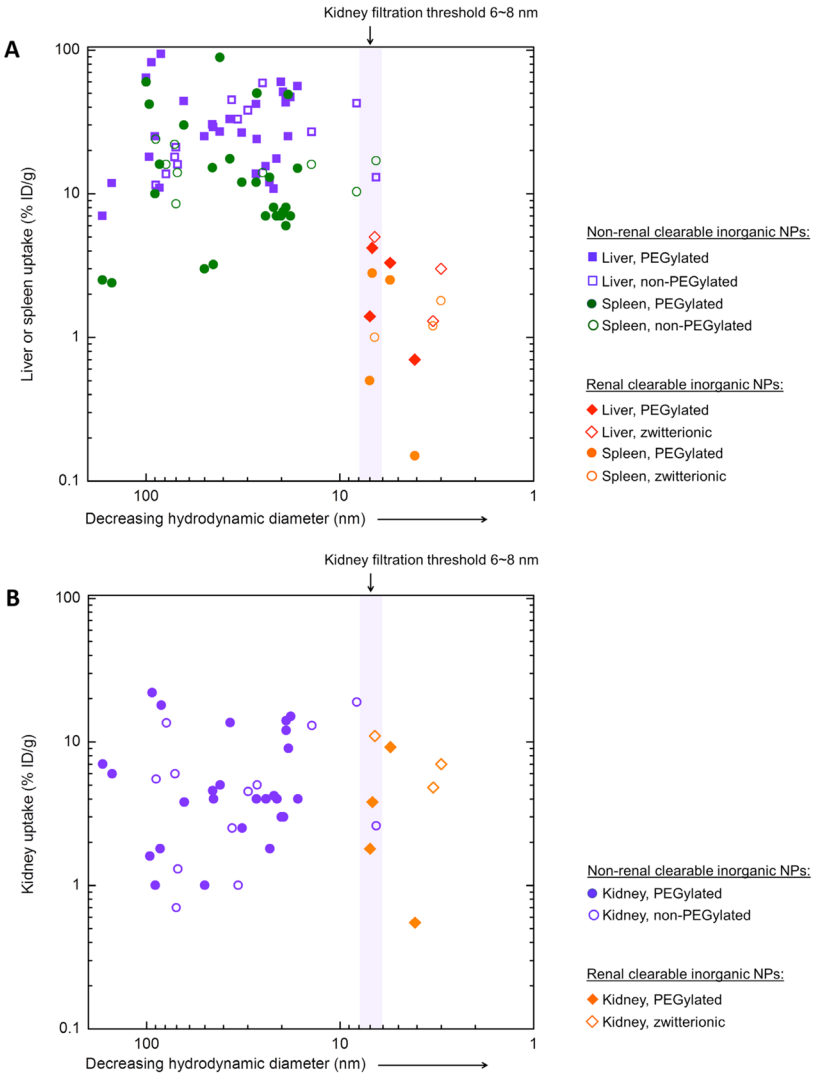

Figure 3. (A) Liver, spleen and (B) kidney uptake of representative nonrenal clearable inorganic NPs and renal-clearable inorganic NPs in mice following intravenous injection. The data are obtained from 29 references that report the biodistribution of various types of nonrenal clearable inorganic NPs with or without PEG-coated surface (gold nanomaterials,[26−31] QDs,[32−37] iron oxide NPs,[38−41] lanthanide upconversion NPs,[42−45] silica NPs,[46] and carbon nanomaterials[47,48]) and renal clearable inorganic NPs (silica NPs,[49] Au NPs,[22,50−52] and carbon dots[53]). Data values and detailed information about the NPs (chemical composition, surface coating, shape, core size, hydrodynamic diameter, biodistribution, application and method for quantifying biodistribution) are presented in Supporting Information Table S2. For the nonrenal clearable inorganic NPs shown in this figure, the average values of liver and spleen uptake are ~30% ID/g ($N = 41$). For renal clearable inorganic NP, the mean and standard deviation values of liver and spleen uptake are 2.7 ± 1.6 and 1.4 ± 1.0% ID/g, respectively ($N = 7$). The kidney uptake of renal clearable inorganic NPs is generally below 12% ID/g (5.5 ± 3.8% ID/g, $N = 7$), comparable or even lower than that of nonrenal clearable NPs in the range of 0.7−22% ID/g (6.4 ± 5.6% ID/g, $N = 39$). Notes: (a) Criteria for selecting representative results: (1) hydrodynamic diameters were reported; (2) biodistribution data was obtained from tumor murine models; (3) biodistribution and tumor targeting efficiency are presented in the unit of % ID/g. (b) Levels of the accuracy of biodistribution data vary according to the quantification methods. The highest level of data accuracy is provided by inductively coupled plasma mass spectrometry (ICP-MS) that can be used to directly measure the elements of NPs. Labeling NPs with radioisotopes and fluorescent dyes may influence data accuracy due to potential dissociation of the labels from the NPs *in vivo*. Data obtained from fluorescence imaging is considered semiquantitative. These data are measured from different xenograft tumor models; 24 h post injection is the most frequently used time point for biodistribution study, and other time points are 4, 12, and 48 h; only one study was performed at 72 h p.i.

nonhuman primates, more than 90% ID of CdSe/CdS/ZnS QDs remained in the major organs including liver and spleen at 90 days post iv injection.[69] CdSe-ZnS QDs with ligand-stabilized surface were found to retain in the body for at least 2 years; some of them remained intact and showed the fluorescence.[70] For other NPs that can decompose inside the macrophages such as lanthanide upconversion nanoparticles (UCNPs),[71] silica NPs[72] and iron oxide NPs,[73] bile excretion was observed after RES uptake but the elimination was very slow (weeks to months) compared with renal clearance of small molecular probes (hours to days).

Excretion Pathway of Renal Clearable Nanoprobes. To address this long-term challenge, severe and long-term

TABLE 1. Design of Recently Developed Renal Clearable Inorganic Nanoparticles and Their Renal Clearance Efficiencies Following Intravenous Administration

core structure	surface ligand	core size/HD (nm)	renal clearable efficiency	imaging modality	ref.
Ultrasmall Core + Protein-Adsorption-Resistant Zwitterionic Surface					
CdSe/ZnS	Cysteine	2.85/4.36	75% ID in 4 h p.i.	Fluorescence	3
CdSe/ZnCdS	cRGD-cysteine (active targeting)	3.4/5.5	>65% ID in 4 h p.i.	Fluorescence	6
CdSe/ZnCdS	GPI-cysteine (active targeting)	3.4/5.5	>65% ID in 4 h p.i.	Fluorescence	6
AuNPs	GSH	1.7/2.1	>50% ID in 24 h p.i.; 65% ID in 72 h p.i.	Fluorescence/CT	50
AuNPs, ^{198}Au-doped	GSH	2.6/3.0	>50% ID in 48 h p.i.	Fluorescence/SPECT	93
AuNPs[a]	GSH	1.2/NR[d]	>60% ID in 8 h p.i.	Fluorescence	94
AuNPs	^{111}In-DTDTPA	2.4/6.6	64% ID in 24 h p.i.	Fluorescence/SPECT	52
Pd nanosheets	GSH	4.4 × 1.8/NR	6.6% ID in 24 h p.i.; 30.9% ID in 15 day p.i.	Fluorescence	78
CuNPs, ^{64}Cu-doped	GSH	2.0/2.2	62.5% ID in 2 h p.i.; 78.5% ID in 48 p.i.	Fluorescence/PET	77
Gd-embedded IONPs	Dopamine sulfonate	4.8/5.2	NR	MRI	53
Ultrasmall Core + Protein-Adsorption-Resistant PEGylated Surface					
Silica NPs (Cornell dots)	PEG_{500}	NR/3.3	73% ID in 48 h p.i.	Fluorescence	76
Silica NPs (Cornell dots)	^{124}I-cRGD-PEG_{500} (active targeting)	NR/6.8	26% ID in 4 h p.i.; 72% ID in 72 h p.i.	Fluorescence/PET	49
AuNPs	PEG_{1000}	2.3/5.5	>50% ID in 24 h p.i.	Fluorescence	52
AuNPs	FA-PEG_{1000}-GSH	2.0/6.1	NR	Fluorescence	92
Au nanoclusters, ^{64}Cu-alloy[b]	PEG_{350}	2.8/4.29	~30% ID in 24 h p.i.	PET	83
Carbon dots	ZW800-PEG_{1500} and/or ^{64}Cu-DOTA-PEG	3/4.1	270% ID/g in 1 h p.i.	Fluorescence/PET	95
Nanographene sheets, ^{125}I-labeled[b]	PEG	10−30/NR	~7.6% ID/g in 24 h p.i.	NR	82
Biodegradable Large NPs					
Porous silicon NPs[c]	NR	NR/126	NR	Fluorescence	80
DNA-assembled AuNP superstructures (core−satellite)[c]	Core: DNA; Satellite: DNA, PEG_{1000}	Core: 13 nm; Satellite: 3 nm	2% ID in 48 h p.i.	Fluorescence	81
Unknown Urinary Excretion Mechanism					
Gd-encapsulated carbon dots	COOH	12/12	NR	MRI	95

[a] The NPs were administered through subcutaneous injection. [b] The NPs were excreted through both renal and hepatic routes. [c] Excretion of the NPs involves a process of cellular uptake and intracellular degradation in liver and spleen. [d] NR = not reported.

accumulation in RES, of nanoprobes in their clinical translation, renal clearable inorganic nanomaterials have recently been developed (Table 1).[8] In 2006, renal excretion route of inorganic materials was first observed by Kostarelos and co-workers in single-walled carbon nanotubes (SWNTs), the one-dimensional nanomaterials with average diameter of 1 nm and average length of 300−1000 nm.[74] In 2007, Choi and co-workers reported the first example of renal clearable spherical inorganic NPs, cysteine-coated CdSe/ZnS core−shell QDs.[3] Using the QDs as a model system, they investigated the requirements for urinary excretion of spherical metal NPs and found the renal clearance threshold was 5.5 nm,[3] very similar to that of proteins.[75] Over the past 8 years, efficient renal elimination has been achieved by silica NPs,[76] gold NPs,[50] carbon dots,[53] iron oxide NPs,[77] palladium nanosheets,[78] and copper NPs.[79] The total 24-h urinary excretion of these renal clearable inorganic NPs are generally >50% ID, comparable to renal clearance efficiencies of the clinically used small molecular probes (Figure 2). For glutathione-coated Pd nanosheets, 6.6 and 30.9% ID are detected in urine in 24 h and 15 days p.i., indicating relatively slow elimination. Because of efficient urinary excretion, the average values of liver and spleen uptake of these renal clearable NPs are only 3.9 ± 2.6 and 1.1 ± 0.9% ID/g at 4−48 h p.i. (N = 11), respectively, 10−30 times lower than those of conventional nonrenal clearable NPs (Figure 3A and Supporting Information Table S2). Kidney is the primary organ for eliminating the renal clearable NPs. At 5 min after iv injection of GS-AuNPs, kidney was the organ showing the highest NP accumulation (~21.4% ID/g); the kidney uptake dropped to ~7.5% ID/g at 1 h p.i. and ~5.1% ID/g at 48 h p.i., suggesting the NPs can pass the kidney and enter to urine without being trapped in the kidney. Therefore, kidney accumulation of the reported renal clearable inorganic NPs is generally below 12% ID/g (5.5 ± 3.8% ID/g, N = 7) at 4−24 h p.i., comparable or even less than that of nonrenal clearable NPs in the range of 0.7−22% ID/g (6.4 ± 5.6% ID/g, N = 39) at 4−48 h p.i. This phenomenon is significantly

different from the nonrenal clearable Au nanomaterials that severely (>30% ID/g) and long-time (months to years) accumulate in the liver and spleen, the organs for excretion of these NPs. Biodegradable silicon NPs[80] and nanoassemblies[81] are also developed to accelerate the body clearance of NPs through urinary excretion (Table 1). In addition, shifting the excretion pathway from the hepatic to renal route becomes feasible for graphene,[82] ^{64}Cu−Au alloy nanoclusters,[83] and UCNPs,[42,62] although the hepatic excretion still dominates. These inorganic nanomaterials with efficient renal excretion shared some common features in design, which were listed as follows.

Reducing Core Size (or Diameter of One-Dimensional Nanomaterials) Below 6 nm. The renal pathway relies on glomerular filtration slit in the kidneys, and the NP size plays a key role in the filtration efficiency. The filtration-size threshold of glomerular capillary walls is typically 6−8 nm; thus, to make inorganic NPs renal clearable, reducing particle size is the first principle to enhance their renal clearance efficiency. After decades, most of inorganic NPs with core size (or diameter for one-dimensional nanomaterilas such as SWNTs) below 6 nm can readily be synthesized. Unlike small molecules with well-defined molecular weight, the NPs always have a certain polydispersity in the size. Thus, the observed renal clearance should be considered as an ensemble behavior of different sized NPs. In addition, the efficient renal clearance of SWNTs also involves a shape effect. The flow induces specific alignment of SWNTs, where the long axis of SWNTs points toward the openings of the glomerular capillary pores; as a result, SWNTs pass the glomerular capillary walls.

Developing Protein-Adsorption-Resistant Surface Chemistry. Because of high surface energy of the NPs, once they are introduced into the bloodstream, nearly 3000 different kinds of serum proteins in the blood could interact with the particle surface and form the "protein corona",[84] resulting in dramatic increase of their HDs and initiation of the macrophage uptake in the RES.[64] To minimize the serum protein binding, Choi and co-workers used zwitterionic surface coating and developed the first example of renal clearable inorganic NPs in 2007.[3] The zwitterionic ligand cysteine-coated QDs (core size of 3 nm, HD of 4.9 nm) can be effectively cleared out of the body as intact NPs through the urinary system (>65% ID, 4 h p.i.). To test whether cysteine could be used to enhance the renal clearance of AuNPs, we created 3.5 ± 0.9 nm cysteine-coated AuNPs,[85] which, however, rapidly aggregated to 220 ± 60 nm NPs in phosphate buffered saline. As a result, only 0.10 ± 0.03% ID were found in urine and more than 50% ID were accumulated in the liver and spleen 24 h p.i. To develop renal clearable Au NPs, we used zwitterionic glutathione (GSH, a tripeptide that is abundantly presented in the cytoplasm and has low affinity to serum proteins[86−88]) to minimize the serum protein adsorption of Au NPs.[50,89] The obtained GSH-coated Au NPs (GS-AuNPs; 600 nm-emitting GS-AuNPs: core size of 1.7 nm, HD of 2.1 nm; NIR-emitting GS-AuNPs: core size of 2.5 nm, HD of 3.3 nm) exhibited high resistance to protein binding, and >50% ID can be cleared out through the urinary system 48 h p.i., more than 10−100 times higher than those of the similar sized nonrenal clearable AuNPs.[90] As an effective zwitterionic ligand, GSH enables not only AuNPs but also other ultrasmall metal NPs such as palladium[78] and copper[79] nanomateirals to be excreted through urinary route, suggesting that GSH can serve as a widely applicable surface chemistry to minimize nonspecific accumulation of inorganic NPs in the body. With help from other zwitterionic ligands such as dithiolated polyaminocarboxylate (DTDTPA)[52] and dopamine sulfonate,[77] renal clearable AuNPs are also created. About 64% ID of DTDTPA-coated AuNPs (core size of 2.4 nm, HD of 6.6 nm) is excreted into the urine at 24 h after iv injection and the liver uptake is less than 5% ID.[52] The observed protein adsorption resistance of ultrasmall zwitterionic NPs is often attributed to the positively and negatively charged layers on the NPs that make it highly difficult for serum proteins to bind to particles.[3,21] However, interactions of zwitterionic NPs with serum proteins are still not quantitatively understood due to the lack of theoretical methodologies to predict the binding of serum protein to the NPs with charged surfaces.

While most PEGylated nanoparticles are not renal clearable due to large HDs, recent studies show that amphiphilic PEG molecules with low molecular weight indeed can serve as effective ligands in making ultrasmall inorganic NPs renal clearable. Unlike zwitterionic small molecules that are charged and have well-defined molecular weights, PEG is a synthetic macromolecule with low charge density; as a result, inorganic NPs coated with PEG ligands usually have much thicker stern layers than zwitterionic NPs. Thus, even for ultrasmall inorganic NPs coated with PEG, their HDs are often larger than the kidney filtration threshold due to the large stern layer. For example, after PEGylation, the HDs of 2 nm AuNPs increased to 9−10 nm.[91] Such large increase in the HDs is due to the well-extended conformation of high-density PEG on the particle surface. On the other hand, inorganic NPs capped by PEG with relatively low molecular weight of 500−2000, such as PEG_{500}-coated silica NPs, PEG_{1500}-coated carbon dots,[53] PEG_{1000}-coated near-infrared (NIR) emitting AuNPs,[51] and PEG_{2000}-GS-AuNPs,[92] are renal clearable, which is mainly because of change in the conformation of PEG on particle surface. For instance, the HD of renal clearable PEG-AuNPs developed by our group is 5.5 nm,[51] much smaller than the previous reported HDs (9−10 nm) of nonrenal clearable PEG-AuNPs with ~2 nm core size. The observed small HD of PEG-coated

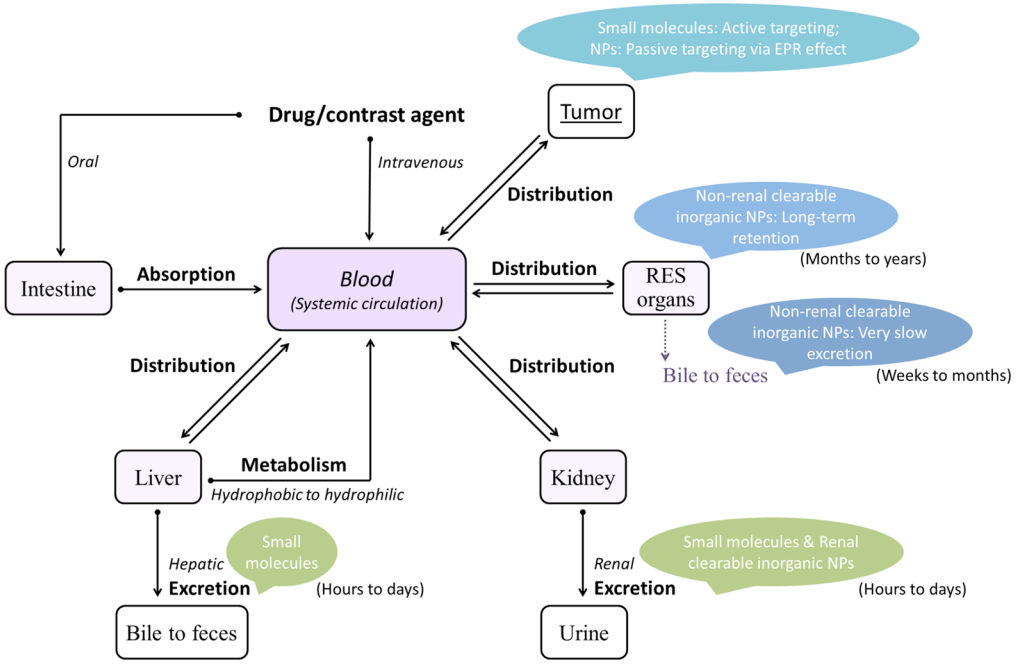

Figure 4. Pharmacokinetics includes absorption, distribution, metabolism, and excretion (ADME) of a drug or contrast agent. The four criteria influence the concentration of the substance and kinetics of the substance exposure to organs/tissues. For intravenous administration, the step of absorption is not involved because the substance is directly introduced to the systemic circulation. The differences in ADME processes between small molecular probes, conventional nanoprobes and molecular nanoprobes are summarized in Figure 1.

NIR emitting AuNPs is due to the coiled conformation of PEG, which decreases the thickness of stern layer. The coiled conformation of surface PEG is formed only when the PEG density on the surface is relatively low, in contrast to the extended conformation of PEG with high density.[13] These results suggested that fine control of density of PEG on the NPs is expected to provide a new pathway to synthesize renal clearable inorganic NPs.

Making Large Nanoparticle Biodegradable. Although efficient renal clearance of NPs can be achievd by decreasing HD below 6−8 nm, some properties of nanoparticles such as NIR emission of QDs and surface plasmon resonance of Au NPs could disappear when the particle size is less than ~5 nm. To maintain the unique properties for cancer imaging while expediting the clearance of large NPs from the body, making larger inorganic NPs degradable provides a possible solution. Using electrochemical etching method, Park and co-workers created the luminescent porous silicon NPs (LPSiNPs, HD of 126 nm).[80] Like conventional large NPs, a majority of the iv injected LPSiNPs accumulated in the liver (~20% ID/g) and spleen (~68% ID/g) at 1 day; however, the liver and spleen uptake of NPs dramatically decreased after 4 weeks (liver, ~3% ID/g; spleen, ~6% ID/g). On the basis of the study of liver and spleen tissues, the clearance mechanism of LPSiNPs involved degradation inside the macrophages (presumably in lysosomes, containing enzymes and with acidic pH) and subsequent release of renal clearable fragments from the cells. Chan and co-workers developed another type of biodegradable NPs, the DNA-assembled superstructures that consisted of a 13 nm AuNP as core and one or two layers of 3 nm renal clearable PEG-AuNPs.[81] Owing to the biodegradability of DNA, the core−satellite superstructures can disassemble to the building blocks after they were internalized by macrophages. Although the majority of superstructures still accumulated in the liver (~45% ID/g at 24 h p.i.), 2% ID of the total Au content was found in mice urine up to 48 h p.i., suggesting a new direction in designing biodegradable inorganic NPs. However, since a process of cellular uptake and intracellular degradation is necessary, the excretion time of these biodegradable NPs is much longer than that of renal clearable inorganic NPs. For instance, the complete clearance of LPSiNPs from body is >4 weeks.[80]

PHARMACOKINETICS (PK)

PK describes a series of processes including absorption, distribution, metabolism and excretion (ADME) that take place in the interaction between an organism and an exogenous substance (a drug or contrast agent) when the exogenous substance is introduced into the body (Figure 4). In most cases, the drug/agent concentration in a body site is closely related to its concentration in systemic circulation. Therefore, to study PK of a contrast agent, blood concentration of the agent is dynamically monitored after administration until the elimination phase and then fitted to obtain key PK parameters such as maximum blood concentration (C_{max}), elimination half-life ($t_{1/2}$), and

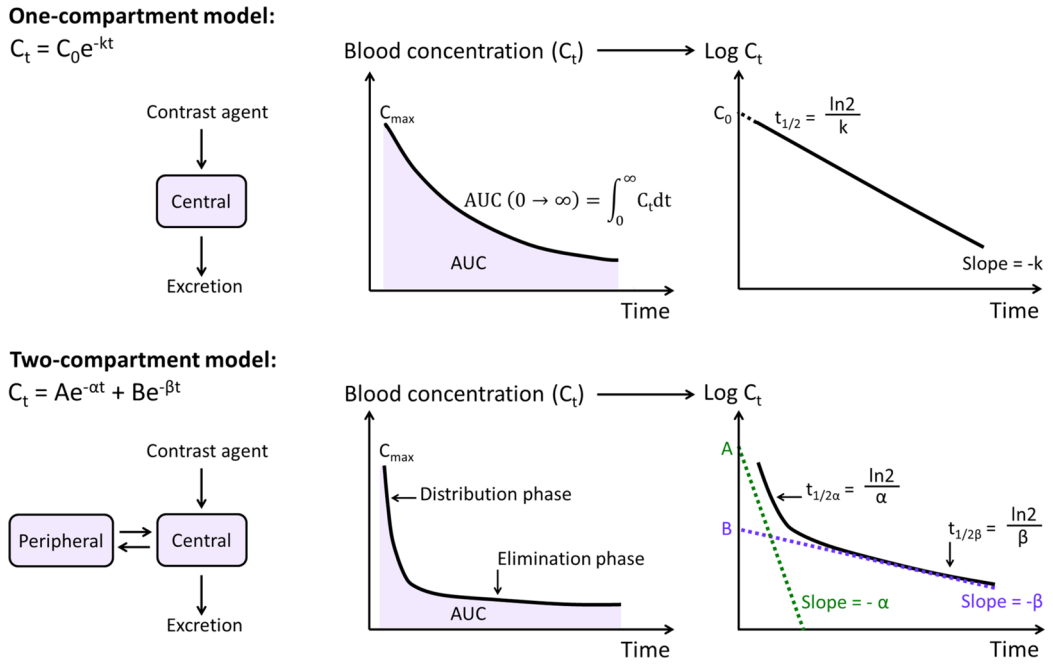

Figure 5. A brief schematic representation of one-compartment and two-compartment pharmacokinetic (PK) models for fitting blood concentration−time curve of a contrast agent following single intravenous injection. The blood concentration reaches the maximum (C_{max}) at the initial time point because the substance is directly introduced to systemic circulation and no absorption step is involved. Central compartment includes blood (systemic circulation) and highly perfused organs such as liver, lung, kidney, *etc*. Peripheral compartment include less perfused tissues such as muscle, fat, *etc*. This figure also shows equations for fitting the blood concentration−time curves and calculating the key PK parameters that influence tumor uptake of contrast agent, such as area under curve (AUC), elimination half-life ($t_{1/2}$) for one-compartment model, and distribution half-life ($t_{1/2\alpha}$) and elimination half-life ($t_{1/2\beta}$) for two-compartment model. Notes: Values of PK parameters may vary depending on the PK modeling methods.

area under the curve (AUC) (Figure 5).[96] These PK parameters of contrast agents can quantitatively reflect the exposure of organs and tissues to the agents and affect not only toxicity but also tumor targeting efficiency.[96] Since extravasation of NPs from tumor vasculature to extracellular tumor microenvironment could be considered an accumulative process, high blood concentration, long blood elimination half-life and large AUC are favorable for enhancing the EPR effect and improving tumor targeting efficiency.[27,51,91,96,97]

The typical pharmacokinetics of small molecular probes is a two-compartment model with a distribution half-life ($t_{1/2\alpha}$) and an elimination half-life ($t_{1/2\beta}$). Both $t_{1/2\alpha}$ and $t_{1/2\beta}$ are very short for some agents with rapid renal excretion ($t_{1/2\alpha}$ < 0.5 h, $t_{1/2\beta}$ < 3−5 h). For instance, after iv injection, the MRI contrast agents gadodiamide (Omniscan), gadopentetate dimeglumine (Magnevist) and gadoteridol (ProHance) can rapidly distribute in the body with $t_{1/2\alpha}$ of 0.07, 0.2, and 0.2 h; their $t_{1/2\beta}$ is 1.3, 1.6, and 1.6 h, respectively, corresponding to more than 90% ID in the urine within 24 h p.i.[16] The $t_{1/2\alpha}$ of CT contrast agents ioxaglate, iomeprol and iodixanol is 0.43, 0.37, and 0.43 h, and the $t_{1/2\beta}$ is 0.93, 1.83, and 2.18 h.[17] In the case of the PET probes [^{18}F]FDG and [^{18}F]fluoromisonidazole ([^{18}F]FMISO) for tumor diagnosis, the $t_{1/2\alpha}$ is 0.09 and 0.06 h, whereas the $t_{1/2\beta}$ is 5.05 and 1.08 h.[24] The $t_{1/2\alpha}$ and $t_{1/2\beta}$ of an organic fluorophore IRDye 800 CW are 0.1 and 1.0 h, respectively.[22] A long elimination half-life of 11.3 h, 10.1 h was observed in [^{18}F]fluoroacetate ([^{18}F]FAc) and ^{99m}Tc-SQ30217, while their distribution half-life is still less than 0.5 h (0.15 and 0.02 h, respectively).

For the PK of conventional nanoprobes, both one-compartment and two-compartment models are observed after iv administration. One-compartment model PK with an elimination half-life of 4−7 h is widely observed in PEGylated inorganic NPs from Au NPs, Ag_2S QDs, UCNPs to SWNTs. During a time period of 0−24 h p.i., the $t_{1/2\beta}$ of 0.3, 5.0, and 3.8 h was detected in the 2 nm Au NPs coated by PEG molecules terminated with negative, neutral, and zwitterionic portion (HD of 9−10 nm), respectively.[91] For PEGylated Ag_2S QDs (core size of 5.4 nm, HD of 26.8 nm), the $t_{1/2\beta}$ was measured to be 4.37 h.[32] $BaYbF_5$: 2% Er^{3+} nanocubes (core size of 9 nm, HD of 22 nm) exhibited a $t_{1/2\beta}$ of 2.2 h.[98] The $t_{1/2\beta}$ of PEGylated $NaGdF_4$ NPs (core size of 5.1 nm) and PEGylated $NaGdF_4$:Yb, Er NPs (core size of 18.5 nm) was 3.0 and 1.1 h, respectively.[42] The SWNTs coated with PEG_{5400} and PEG_{2000} showed the $t_{1/2\beta}$ of ∼2 and ∼0.5 h, respectively.[99] Some PEGylated inorganic NPs show two-compartment model pharmacokinetics. For instance, the $t_{1/2\alpha}$ of UCNPs,[62] iron oxide NPs[38] and graphene[82] is 0.4, 0.3, and 0.39 h, respectively, and their $t_{1/2\beta}$ is 4.3, 3.78, and 6.97 h, respectively (0−24 h p.i.).

In the case of GS-AuNPs, one type of molecular nanoprobes, their PK profile follows a two-compartment model that integrate the advantages of small molecular probes with conventional nanoprobes for tumor targeting: short distribution half-life ($t_{1/2\alpha}$ = 5.4 ± 1.2 min, like small molecular probes) ensures rapid access of each tissue including the tumor region to NPs, and relatively long elimination half-life ($t_{1/2\beta}$ = 8.5 ± 2.1 h, like PEGylated large NPs) allows NPs to circulate in the blood at a relatively high concentration and continuously extravasate from the blood vessels into the tumor (the impaired lymphatic drainage renders the NPs stay in the tumor for long time).[93] While the elimination half-life of renal clearable PEG-AuNPs ($t_{1/2\beta}$ = 9.2 ± 3.9 h) is comparable to that of GS-AuNPs, the distribution half-life extends to 56.1 ± 1.2 min, 10 times longer than that of GS-AuNPs.[51] The effect of pharmacokinetics on the tumor targeting efficiency of renal clearable Au NPs will be discussed in the following section.

PASSIVE TUMOR TARGETING VIA EPR EFFECT

EPR effect is one big strength of nanomedicines in cancer diagnosis and therapy. The concept of EPR effect was first proposed by Maeda *et al.* in 1986 to explain the tumor-selective distribution of protein–polymer conjugates,[100] and has been extended to other macromolecules such as plasma proteins, micelles, liposomes, DNA-complexes and even inorganic NPs.[101] On the basis of the studies of organic macromolecules, the EPR effect is considered as a size-dependent phenomenon: only macromolecucles larger than 40 kDa (>5 nm, nonrenal clearable) can target the tumor *via* the EPR effect;[102] once the molecules are renal clearable, the EPR effect becomes negligible, resulting in low tumor targeting efficiency and rapid clearance from tumor. For example, the tumor targeting efficiencies of small molecules IRDye 800CW and ^{64}Cu-DOTA were only 0.22 and 0.15% ID/g at 12 and 46 h p.i., respectively (Supporting Information Table S2). One reason for this phenomenon is that the rapid renal filtration dramatically decreases the blood concentration, thereby reducing the exposure of tumor to the agents. Therefore, prolongation of blood circulation by avoiding renal excretion and reducing RES uptake is considered as a key to enhance the tumor targeting efficiency.[96] Another reason is the poor retention of small molecules in the tumor because they can be easily pushed back to the blood.[96,103] To extend the tumor retention of small molecules, an effective strategy is to conjugate active targeting ligands (*e.g.*, proteins, peptides, aptamers) or based on a mechanism of selective tumor uptake (the most successful examples is [^{18}F]FDG, the glucose labeled with radioactive ^{18}F). By virtue of enhanced glucose uptake in tumor cells, the targeting efficiencies of [^{18}F]FDG reached 4.59% ID/g in EMT-6 tumor at 1 h p.i., and [26] 9.35% ID/g in KHT sarcoma (Supporting Information Table S2).[24] On the other hand, owing to low accumulation in the liver, the tumor-to-liver ratios of small molecules can be larger than 1 (for example, 7.92 of [^{18}F]FDG and 1.16 of IRDye 800CW), reflecting a relatively low uptake in nontarget organs (Supporting Information Table S2).

Conventional inorganic NPs can escape rapid kidney filtration, while PEG-coated surface can slow down the RES uptake; as a result, their blood retention time and concentrations are much longer and higher than those of small molecules, which render them high tumor targeting efficiencies due to the EPR effect. As shown in the tumor uptake of representative nonrenal clearable inorganic NPs (Figure 6), a majority of the NPs have tumor uptake of 1–15% ID/g at 4–72 h p.i. Through passive tumor targeting *via* EPR effect, tumor targeting efficiency of >7% ID/g is observed in various types of inorganic NPs in tumor xenograft mouse models such as EMT-6 (mouse breast carcinoma), MDA-MB-435 (human melanoma), U-87 MG (human glioblastoma) and 4T1 (mouse breast carcinoma) (Figure 7 and Supporting Information Table S2). For instance, PEG_{5000}-Au nanocages[104] and PEG_{5000}-Au NPs[26] can selectively accumulate in EMT-6 tumor with targeting efficiencies of 15.3 and 12.5% ID/g at 24 h p.i., respectively. For MDA-MB-435 tumor model, the targeting efficiencies of PEG_{5000}-Au nanorods and PEG_{5000}-Au nanohexapods can reach 8.4 and 7.2% ID/g at 24 h p.i., respectively.[105] In the case of 4T1 tumor, targeting efficiency of 8–17% ID/g is observed from SWNTs,[47,106,107] Ag_2S QDs,[32] and Au nanocages.[31] These high tumor targeting efficiency of Au nanomaterials *via* EPR effect in the range of 7–15% ID/g is comparable to or even higher than the targeting efficiencies of [^{18}F]FDG in EMT-6 tumor (4.59% ID/g, 1 h p.i.)[26] and KHT sarcoma (~9.35% ID/g, 4 h p.i.).[24] Ultrahigh tumor accumulation of 20–30% ID/g is found in PEG-SWNTs in 4T1 tumor.

However, PEG coating is found to reduce the cellular interaction of NPs and results in inefficient internalization by the cells;[96] to solve this problem, PEGylated NPs are often conjugated with active targeting ligands. Regarding the same type of PEGylated NPs with and without conjugation of active targeting ligands, many works show that active targeting strategy indeed dramatically enhances the tumor targeting efficiency of NPs compared with passive targeting *via* EPR effect. For example, conjugation of RGD peptide increases the targeting efficiencies of PEG_{3400}-Au tripods,[29] PEG_{2000}-InAs/InP/ZnSe QDs[36] and PEG_{5000}-$NaYF_4$:Yb,Er,Tm NPs[43] in U-87 MG tumor from 2.6, 2.9, and 3.0% ID/g to 7.9, 10.7, and 14.5% ID/g at 24, 4, and 24 h p.i., respectively, corresponding to a 3- to 5-fold increase (Figure 7). On the other hand, weak enhancement of tumor targeting efficiency by active targeting is found in 4T1 tumor model when TRC105 antibody is used as targeting ligands.[46,48] Very recently, Chan and

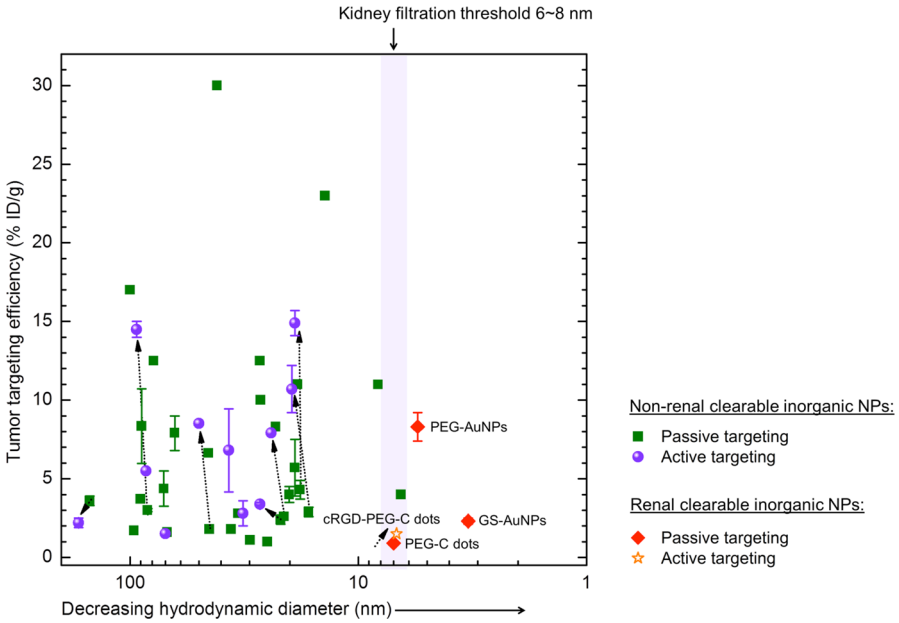

Figure 6. Tumor targeting efficiencies of representative nonrenal clearable inorganic NPs and renal-clearable inorganic NPs in subcutaneous tumor mouse model following intravenous injection. The data are obtained from 26 references that report the tumor targeting behaviors of nonrenal clearable inorganic NPs with or without conjugation of active targeting ligands (active targeting *vs* passive targeting) such as gold nanomaterials,[26−31] QDs,[32−37] iron oxide NPs,[38−41] lanthanide upconversion NPs,[42−45] silica NPs,[46] and carbon nanomaterials.[47,48] Renal clearable inorganic NPs include PEGylated silica NPs (Cornell dots, C dots) with or without cRGD conjugation (cRGD-C dots and PEG-C dots),[49] NIR-emitting glutathione-coated Au NPs (GS-AuNPs)[22] and NIR-emitting PEG-coated Au NPs (PEG-AuNPs).[51] Data values and detailed information about the NPs are presented in Supporting Information Table S2. Arrows are used to connect the passive and active targeting data obtained from the same type of NPs with and without conjugation of active targeting ligand (arrows point from passive targeting to active targeting). Notes: Levels of the accuracy of biodistribution data vary according to the quantification methods. The highest level of data accuracy is provided by inductively coupled plasma mass spectrometry (ICP-MS) that can be used to directly measure the elements of NPs. Labeling NPs with radioisotopes and fluorescent dyes may influence data accuracy due to potential dissociation of the labels from the NPs *in vivo*. Data obtained from fluorescence imaging is considered semiquantitative. These data are measured from different xenograft tumor models; 24 h post injection is the most frequently used time point for biodistribution study; other time points are 4, 12, and 48 h; only one study was performed at 72 h p.i. Results of renal clearable GS-AuNPs and PEG-AuNPs obtained at 12 h p.i. are plotted in this figure.

co-workers systematically studied the effect of NP size on passive and active targeting of NPs by using different-sized spherical Au NPs (15, 30, 60, and 100 nm) and MDA-MB-435 orthotopic tumor xenografts (transferrin served as active targeting ligand).[108] They found active targeting only enhanced the tumor uptake of 60 nm NPs when compared to their passive counterparts; no significant differences were observed for 15, 30, and 100 nm NPs. This result suggests a complexity involved with manipulating active tumor targeting of NPs. Moreover, it is worth pointing out that the high tumor targeting efficiency in U87MG tumor (>7% ID/g), obtained by active targeting strategy, is also achievable for passive targeting *via* EPR effect. The tumor targeting efficiencies of PEG_{5000}-CdSe/ZnS QDs[33] and PEG_{5000}-CuInS/ZnS QDs[34] are measured to be ~11 and 8.3% ID/g in U87MG model at 42 and 48 h p.i., respectively.

Despite the high targeting efficiency, nonrenal clearable nanoparticles even with PEG-coated surface still exhibit severe accumulation in the liver and spleen after circulation (Figure 3A), resulting in low tumor targeting specificities (tumor-to-liver ratios for nonrenal clearable NPs) and raising concern of long-term toxicity of these NPs. For the representative nonrenal clearable nanoprobes, their tumor-to-liver ratios are generally <0.5 and the average value is ~0.28 (Figure 8A). For the active and passive tumor targeting strategies, there is no significant difference in the tumor-to-liver ratio (passive targeting, ~0.29; active targeting, ~0.28; $p > 0.05$).

Switching the excretion route of inorganic NPs from hepatic elimination to renal pathway provides a solution to accelerate particle clearance from the body but naturally raises a fundamental question of whether renal clearable inorganic NPs still exhibit tumor-selective distribution and long retention *via* the EPR effect, like the nonrenal clearable NPs. By analyzing the reported results of tumor targeting with renal clearable inorganic NPs, we found that the two seemingly contradictory properties, efficient renal clearance and EPR effect, indeed can be integrated in renal clearable NIR-emitting GS-AuNPs[22] and PEG-AuNPs,[51] although the EPR effect in some renal clearable inorganic NPs is negligible or weak. On the basis of tumor targeting efficiency and retention time in tumor, the currently reported renal clearable inorganic NPs can be divided into three groups with different levels of EPR effect.

Renal Clearable Inorganic NPs with Weak EPR Effect. The PEGylated ultrasmall silica NPs (Cornell dots, C dots) are

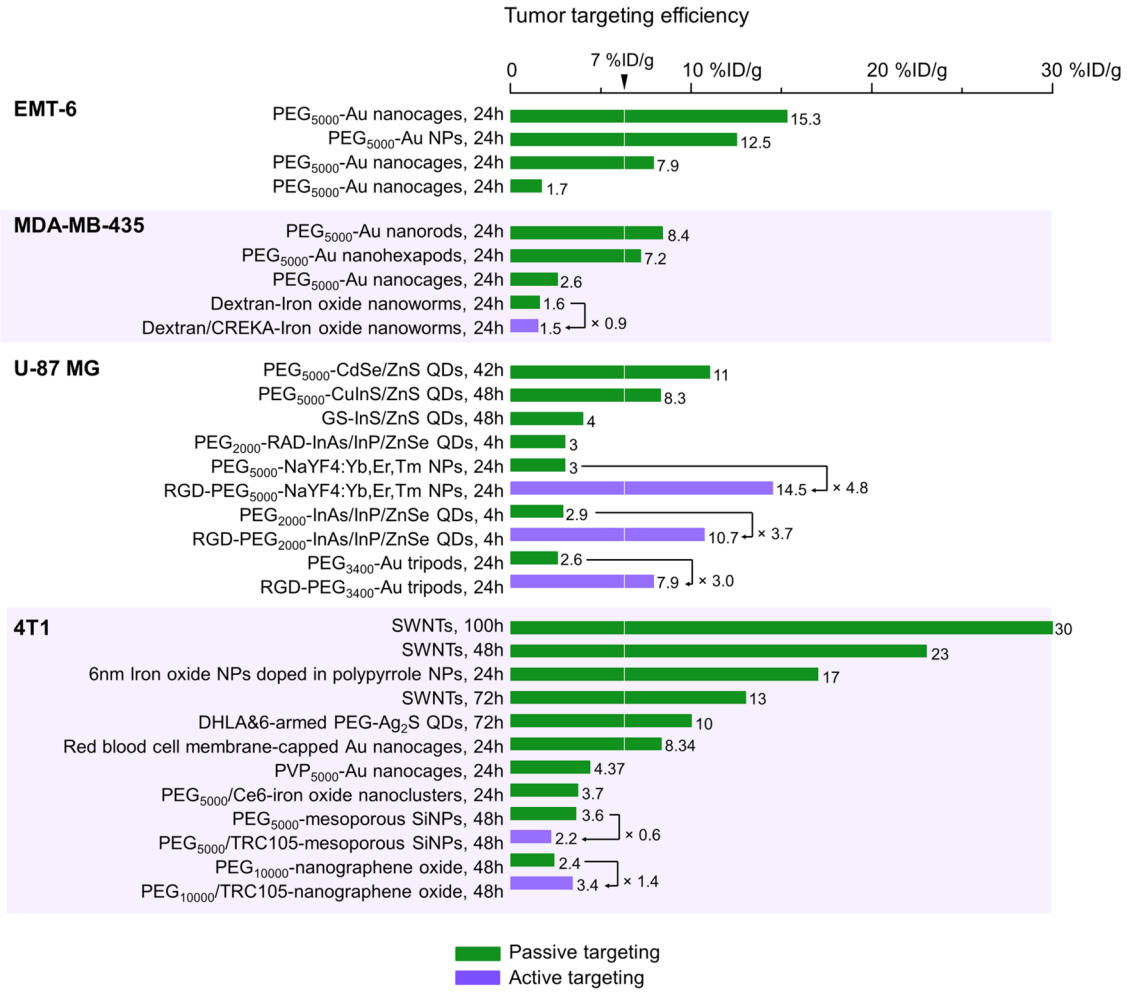

Figure 7. Tumor targeting efficiencies of representative nonrenal clearable inorganic NPs in tumor xenograft mouse models EMT-6 (mouse breast carcinoma), MDA-MB-435 (human melanoma), U-87 MG (human glioblastoma) and 4T1 (mouse breast carcinoma) following intravenous injection. The data are obtained from references cited in Figure 6 that report the tumor targeting behaviors of nonrenal clearable inorganic NPs with or without conjugation of active targeting ligands (active targeting *vs* passive targeting). Data values and detailed information about the NPs are presented in Supporting Information Table S2. Arrows are used to connect the passive and active targeting data obtained from the same type of NPs with and without conjugation of active targeting ligand (arrows points from passive targeting to active targeting).

the first renal clearable inorganic nanoprobes that entered clinical trial.[109] As previously found in preclinical study using M21 (human melanoma) tumor-bearing mice, targeting efficiency of PEG-C dots was only 0.9% ID/g at 4 h p.i. then decreased to ~0.25% ID/g at 24 h p.i., suggesting the EPR effect is indeed negligible.[49] After conjugation with c-RGD peptide, an active targeting ligand, the targeting efficiencies in the M21 tumor can increase to 1.5% ID/g at 4 h and ~1.0% ID/g at 24 h p.i., still much lower than the tumor uptake of conventional NPs with strong EPR effect (7−15% ID/g, without active targeting ligands, Figures 6 and 7, Supporting Information Table S2). In a recent clinical study of ^{124}I-labeled cRGD-PEG-C dots for PET imaging, the NP uptake was observed to circumscribe the metastatic tumor in the liver with low imaging contrast (at 4 h p.i.), which was very different from the tumor area visualized with [^{18}F]FDG (Figure 9A−C,E).[109] After 24 h p.i, ^{124}I-labeled cRGD-PEG-C dots were eliminated from the tumor, indicating a short retention of NPs in the tumor (Figure 9D). Clearance of renal clearable NPs from tumor area within 24 h was also seen in the dye-labeled carbon dots.[53] Using the ZW800/PEG-carbon dots, the SCC-7 tumor on mouse was detected at 2 h p.i. but failed to be distinguished from surrounding normal tissue at 24 h p.i. (Figure 9F).

Similar to C dots, renal clearable cysteine-QDs[6] and Gd-encapsulated carbon dots (Gd@carbon dots)[95] also rely on the active targeting strategy to enhance tumor uptake. The contrast of U-87 MG tumor on MR images can be enhanced with RGD-conjugated Gd@carbon dots from 1 at prescan to ~1.3 at 4 h p.i.; however, no significant change in the tumor contrast was observed within 4 h p.i. after injection of renal clearable Gd@carbon dots free of RGD (Figure 9G,H).[95] One possible reason for the negligible EPR effect of these renal clearable NPs is rapid elimination from the blood pool through urinary excretion. Pharmacokinetics studies revealed the

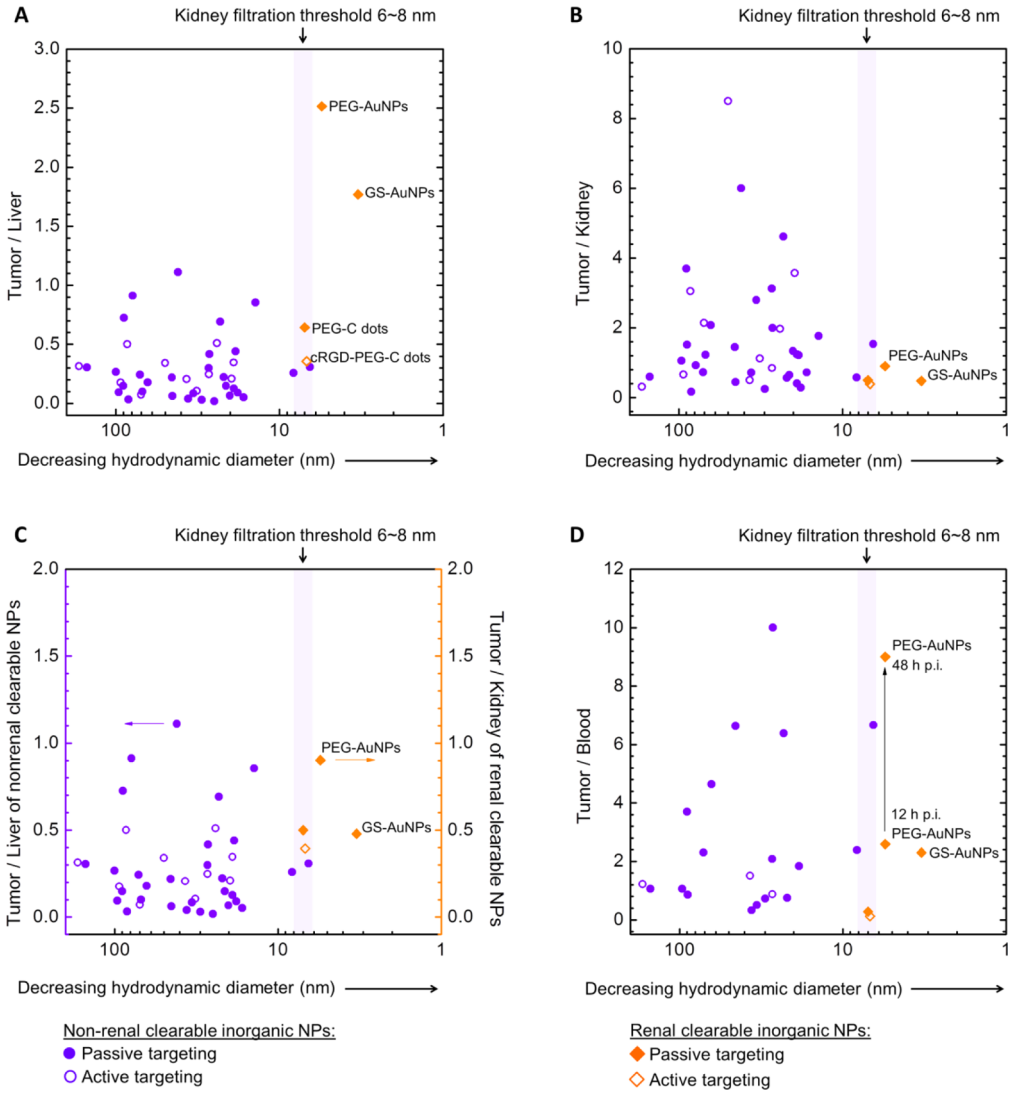

Figure 8. (A and C) Tumor-to-liver, (B and C) tumor-to-kidney and (D) tumor-to-blood ratios of representative nonrenal clearable inorganic NPs and renal-clearable inorganic NPs in subcutaneous tumor mouse model following intravenous injection. (C) Since liver and kidney are the major accumulation sites of nonrenal clearable and renal clearable NPs, respectively, "tumor targeting specificity" is defined as tumor-to-liver ratio for nonrenal clearable NPs and tumor-to-kidney ratio for renal clearable NPs. The data are obtained from references cited in Figure 6 that report the tumor targeting behaviors of nonrenal clearable inorganic NPs with or without conjugation of active targeting ligands (active targeting *vs* passive targeting). Data values and detailed information about the NPs are presented in Suppoprting Information Table S2. Results of renal clearable GS-AuNPs and PEG-AuNPs obtained at 12 h p.i. are plotted in A–D; data of PEG-AuNPs obtained at 48 h p.i. is also included in D.

blood elimination half-life of cysteine-QDs is 0.8 h and less than 1% ID/g of the renal clearable QDs was found in the blood at 4 h p.i.[3] In addition, they are relatively rapidly cleared from the tumor, like the small molecules.

Renal Clearable Inorganic NPs with Moderate EPR. While the EPR effect is significantly reduced in renal clearable silica NPs, QDs, and carbon dots as discussed above, we recently demonstrate that it is possible to make the EPR effect retained in the renal clearable Au NPs.[22] Significantly different from the renal clearable silica NPs, QDs and carbon dots showing low tumor uptake and short tumor retention time (Figure 9), GS-AuNPs exhibited typical tumor targeting behaviors of nanoprobes with EPR effect: enhanced tumor uptake, prolonged tumor retention, and increase of tumor contrast over time (Figure 10A–E). We conducted a head-to-head comparison of renal clearable NIR-emitting GS-AuNPs and a renal clearable NIR organic fluorophore, IRDye 800 CW, in tumor targeting. As found by *in vivo* fluorescence imaging of mice bearing MCF-7 tumor (human breast carcinoma), the two probes behaved similarly in the initial stage of tumor targeting: a rapid distribution to the whole body was observed in the mice after iv injection (Figure 10A,B), and the tumor intensity reached maximum values within 40 min (Figure 10C). However, their retention times in the tumor and normal tissues are significantly different (Figure 10B,C). IRDye 800 CW was rapidly eliminated from both normal tissues (half-life of 2.3 h) and tumor areas (half-lives of 1.4 (70.7%)/6.2 h (29.3%)).

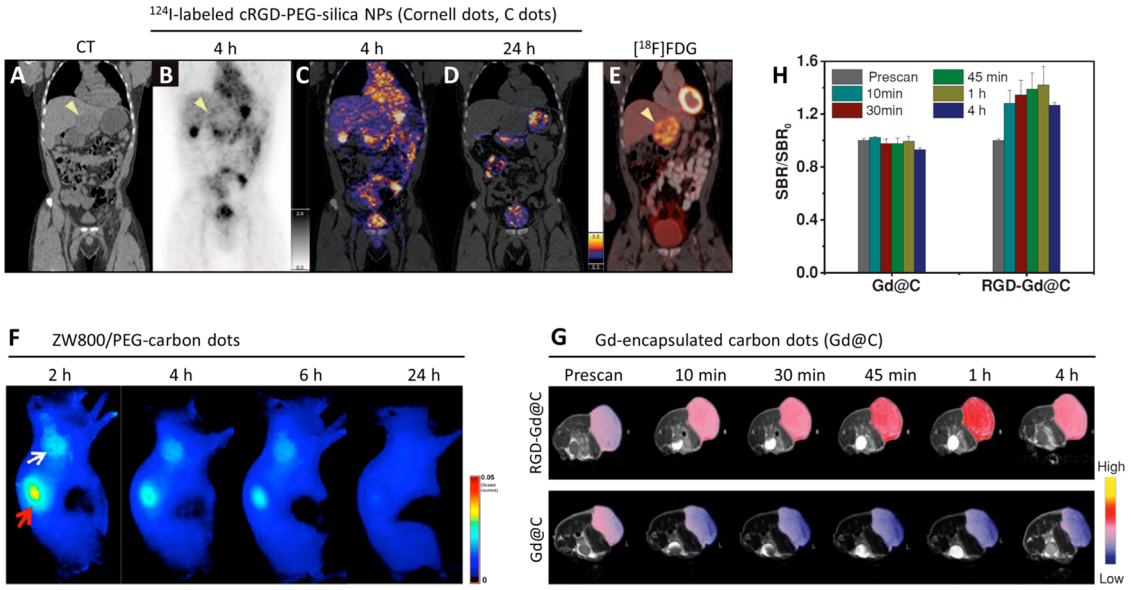

Figure 9. Tumor imaging of renal clearable inorganic NPs with weak EPR effect. (A−E) Application of ^{124}I-labeled cRGD-PEG-C dots in clinical cancer imaging. (A) CT image and (E) [^{18}F]FDG PET image of a patient having anorectal mucosal melanoma identified a liver metastasis within the inferior left lobe (arrowhead). (B,C) Peripheral aspect of the metastatic tumor (arrowhead) showed up on the PET images after iv injection of ^{124}I-labeled cRGD-PEG-C dots at 4 h p.i., (D) but disappeared at 24 h p.i. PET and CT images are overlapped and shown in C and D. Reprinted with permission from ref 109. Copyright 2014 The American Association for the Advancement of Science. (F) NIR fluorescence images of SCC-7 tumor (mice squamous cell carcinoma) bearing mouse at 2−24 h post iv injection of ZW800/PEG-carbon dots (white arrow marks tumor; red arrow indicates kidney). Reprinted with permission from ref 53. Copyright 2013 American Chemical Society. (G) T_1-weighted coronal MR images of U-87 MG tumor (human glioblastoma) bearing mice after iv injection of Gd-encapsulated carbon dots (Gd@C, passive tumor targeting) and c(RGDyK) peptide-conjugated Gd@C (RGD-Gd@C, active tumor targeting). Tumor areas are displayed in color. (H) With Gd@C or RGD-Gd@C as contrast agent, the relative change of signal-to-background ratio (SBR) of tumor areas compared with that of prescan (SBR_0). Reprinted with permission from ref 95. Copyright 2014 WILEY-VCH Verlag GmbH & Co. KGaA, Weinheim.

At 24 h p.i., less than 5% of the maximum intensity of IRDye 800 CW was detected in the tumor, indicating most of dye molecules were cleared from the tumor. In contrast, the fluorescence intensity of GS-AuNPs in the tumor remained constant at ~90% of maximum value during 5−24 h p.i., whereas more than 90% of the NPs were cleared from the normal tissue with a half-life of 43.4 min. Owing to the tumor-selective distribution of GS-AuNP, the tumor area was detectable on fluorescence image at 3 h p.i., and became even more clearly evident at 12 h p.i. (Figure 10A), corresponding to a continuous increase of tumor contrast index (CI) after iv injection of GS-AuNPs (Figure 10D, CI = (fluorescence intensity of tumor area − autofluorescence)/(fluorescence intensity of normal contralateral region − autofluorescence)[110]). Such an increase of tumor contrast over time originates from long retention of probes in the tumor and rapid clearance from surrounding normal tissues, and is regarded as a typical characteristic of tumor targeting through the EPR effect.[111] The accumulations of GS-AuNPs in the MCF-7 tumor were measured to be 3.2 and 2.3% ID/g at 1 and 12 h, respectively. The tumor uptake of GS-AuNPs remained at 2.5% ID/g at 24 h p.i., confirming the long tumor retention.[51] These findings indicate the EPR effect does exist for GS-AuNPs even if they are renal clearable. The origin of enhanced EPR effect in renal clearable GS-AuNPs is because these NPs can evade the uptake of the RES organs, but their renal excretion is relatively slow, thus exhibiting a relatively long elimination half-life of 8.5 h, 10 times the elimination half-life of renal clearable cysteine-QDs. GSH-coated palladium nanoplates, which were found to be slowly cleared from the body into urine during 15 days after injection, can target 4T1 tumor with an efficiency of 5% ID/g.[78]

Renal Clearable Inorganic NPs with Strong EPR. Optimizing the pharmacokinetics can further enhance the tumor accumulation of renal clearable inorganic NPs through the EPR effect. Since PEG ligands are well-known for their capability to prolong blood circulation time, we created renal clearable PEGylated NIR-emitting AuNPs.[51] Due to their hydrophobicity and low charge density, PEGylated NPs often have much larger HDs than zwitterionic NPs and the HD of NIR-emitting AuNPs coated with 1 kDa PEG reached 5.5 nm, close to kidney filtration threshold. A long retention of these PEG-AuNPs in the tumor was detected by *in vivo* fluorescence imaging of mice bearing MCF-7 tumors (Figure 10F−I). At 5 h p.i., the tumor area became visible, and the high quality image with tumor contrast index >2.5 was obtained at 12 h p.i. and maintained until 48 h p.i. (Figure 10F,G). Different from GS-AuNPs, the tumor intensity decreased after reaching the peak value at ~6 h p.i., suggesting the PEG-AuNPs were partially cleared from the tumor area (Figure 10H).

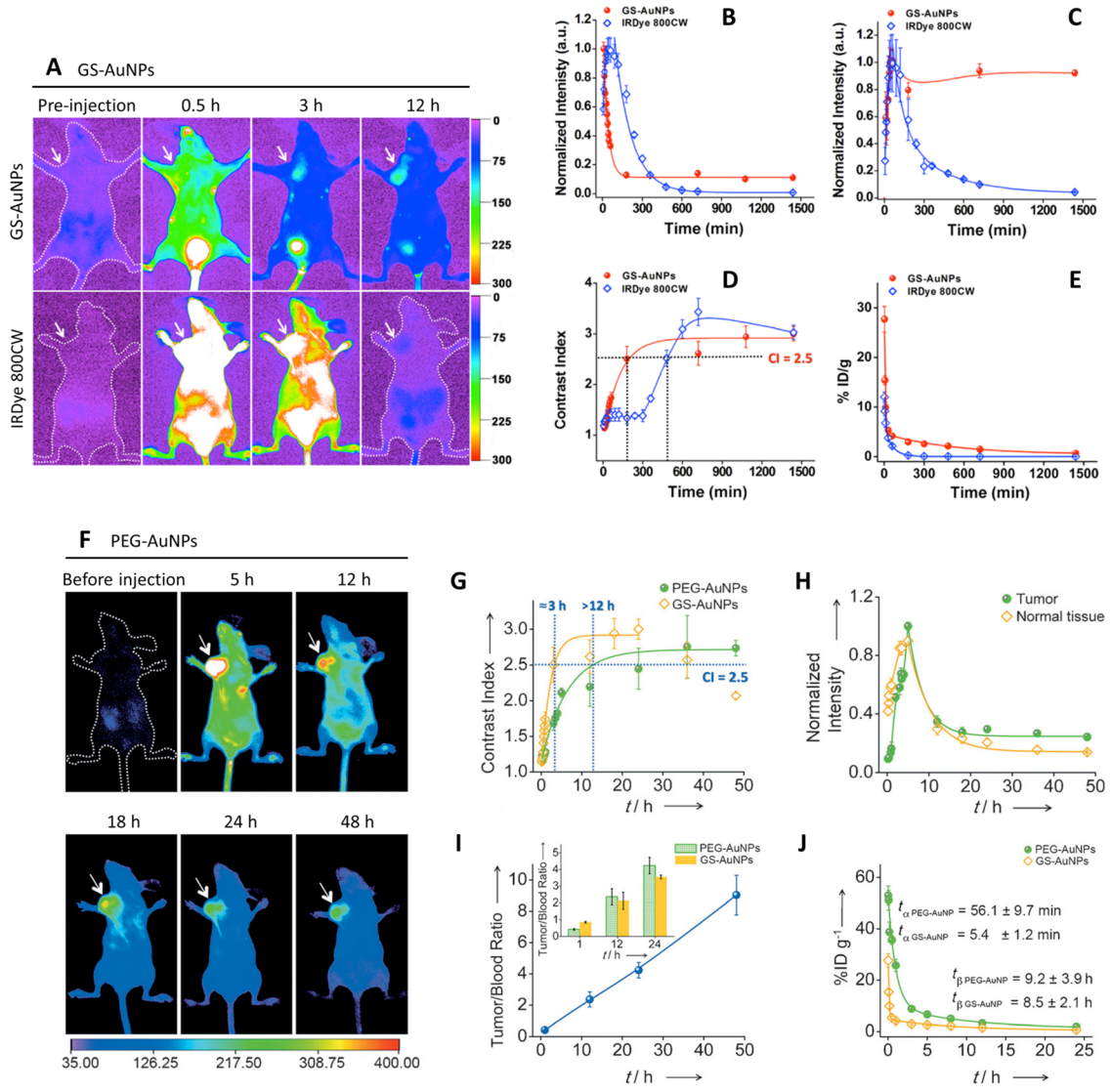

Figure 10. Tumor imaging of renal clearable inorganic NPs with (A−E) moderate and (F−J) strong EPR effect. (A) NIR fluorescence images of mice bearing MCF-7 tumor (human breast carcinoma) following iv injection of GS-AuNPs and IRDye 800CW (arrow indicates the tumor location). (B) Accumulation and retention kinetics of the two probes in normal tissue and (C) tumor 0−24 h p.i. (D) Time-dependent contrast index of tumor after probe injection. (E) Pharmacokinetics of GS-AuNPs and IRDye 800CW (0−24 h p.i.). Reprinted with permission from ref 22. Copyright 2013 American Chemical Society. (F) NIR fluorescence images of MCF-7 tumor-bearing mouse iv injected with PEG-AuNPs (arrow indicates the tumor location). (G) Time-dependent contrast index of tumor after iv injection of PEG-AuNPs and GS-AuNPs. (H) Accumulation and retention kinetics of PEG-AuNPs in tumor and normal tissues 0−24 h p.i. (I) Time-dependent tumor/blood ratio of PEG-AuNPs 0−48 h p.i. (Inset: tumor/blood ratios of GS-AuNPs and PEG-AuNPs at 1, 12, and 24 h p.i.). (J) A comparison of pharmacokinetics of GS-AuNPs and PEG-AuNPs after iv injection (0−24 h p.i.). Reprinted with permission from ref 51. Copyright 2013 WILEY-VCH Verlag GmbH & Co. KGaA, Weinheim.

The tumor-targeting efficiency of PEG-AuNPs was measured to be 8.0 ± 1.5 and 8.3 ± 0.9% ID/g at 1 and 12 h p.i., 3 times higher than that of renal clearable GS-AuNPs and comparable to that of non-renal clearable inorganic NPs such as PEGylated 20 nm AuNPs (6.63% ID/g),[27] PEGylated Au nanocages (7−15% ID/g),[56] and six-armed PEGylated Ag_2S QDs (10% ID/g).[32]

The origin of such a high tumor-targeting efficiency of these PEG-AuNPs is attributed to the strong EPR effect enhanced by extended distribution half-life and increased AUC of the NPs. The tumor-to-blood ratio, a typical parameter for quantifying EPR effect, of PEG-AuNPs, monotonously increased with time and reached 9.0 ± 1.3 at 48 h p.i. (Figure 10I), comparable to many known nonrenal clearable NPs with strong EPR effect (Figure 8D and Supporting Information Table S2). The $t_{1/2\alpha}$ of PEG-AuNPs was 56.1 ± 9.7 min, one order longer than that of GS-AuNPs (5.4 ± 1.2 min), while the $t_{1/2\beta}$ of PEG-AuNPs (9.2 ± 3.9 h) was comparable to that of GS-AuNPs (8.5 ± 2.1 h). In addition, AUC of PEG-AuNPs (142.8% ID·h/g) was 3 times larger than that of GS-AuNPs (47.2% ID·h/g) over 24 h p.i. (Figure 10J). Such large AUC of PEG-AuNPs in the blood

is fundamentally responsible for the large enhancements in tumor targeting efficiency. Moreover, different from renal clearable GS-AuNPs that show long retention in the tumor (targeting efficiency is maintained at ~2.3% ID/g from 12 to 24 h p.i.), the tumor targeting efficiency of PEG-AuNPs decreased from ~8% ID/g at 12 h p.i. to ~4.5% ID/g at 24 h p.i. The reason might be the reduced cellular interaction of NPs that is observed in nonrenal clearable PEGylated NPs.

SYNERGY OF RENAL CLEARANCE AND EPR EFFECT IN CANCER IMAGING

Successful integration of efficient renal clearance and the EPR effect renders inorganic NPs some unique strengths in cancer imaging: improved tumor targeting specificity (defined as tumor-to-kidney ratio for renal clearable NPs), high tumor-to-liver ratio, rapid tumor detection, and low background in liver and gastrointestinal tract. The tumor targeting specificity (tumor-to-kidney ratio) of renal clearable PEG-AuNPs at 0.90 is higher than the tumor targeting specificities (tumor-to-liver ratios) of the majority of nonrenal clearable NPs (<0.5, Figure 8C and Supporting Information Table S2). The tumor-to-kidney ratio of PEG-AuNPs is also comparable to those of some nonrenal clearable NPs (Figure 8B and Supporting Information Table S2). Since accumulation of GS-AuNPs in liver is more than 10 times lower than that of large AuNPs (30−60% ID/g), the tumor-to-liver ratio of GS-AuNPs (1.77) is one or two orders larger than that of nonrenal clearable AuNPs (Figure 8A and Supporting Information Table S2). The tumor-to-liver ratio of renal clearable PEGylated AuNPs of 2.52 at 12 h p.i. is higher than that of GS-AuNPs,[22] suggesting that PEGylation of renal clearable AuNPs could further enhance tumor-targeting efficiency without sacrificing high tumor-to-liver ratio.

Imaging contrast is the key factor determining sensibility in imaging-based diagnostic technique. In the case of tumor imaging, although tumor uptake of NPs can be enhanced through different strategies, high tumor targeting efficiency does not always lead to high imaging contrast. To improve the tumor contrast, one effective approach is to reduce background. Choi and co-workers demonstrated that introducing zwitterionic properties into NIR fluorophores can greatly enhance the tumor-to-background ratio by lowering the background.[112] Consistent with this finding, our studies show that the high tumor contrast obtained with GS-AuNPs was also contributed from the background reduction. GS-AuNPs with zwitterionic surface were eliminated from the background tissues 3 times faster than the small dye molecule IRDye 800 CW. Combining the rapid clearance and prolonged retention in the tumor area, GS-AuNPs took 3.1 ± 0.2 h to reach a contrast index value of 2.5, a threshold for substantial tumor detection, whereas IRDye 800 CW took 8.2 ± 0.6 h. These findings indicate that renal clearable NIR-emitting GS-AuNPs are more suitable for rapid tumor detection than NIR dyes in fluorescence cancer imaging.

Furthermore, the low accumulation of inorganic NPs in RES organs offers a minimized background in the liver and spleen, which is beneficial not only to image primary and metastatic tumors in these organs but also to minimize interference in other diagnostic tests and as well as to improve contrast during fluorescence-guided surgery. Urinary excretion of probes also avoids the contamination of the gastrointestinal tract, thus allowing for the fluorescence-guided surgery in the abdomen.[21]

CONCLUSION AND FUTURE PROSPECTIVE

The EPR effect, observed from tumor targeting of polymeric/biological macromolecules, has been considered as a privilege of nonrenal clearable NPs. Until very recently, both the efficient renal clearance and EPR effect are observed in some ultrasmall inorganic NPs. To summarize the characteristic *in vivo* behaviors of these renal clearable inorganic NPs with EPR effect, we propose a concept of "molecular nanoprobes" that refers to a new type of contrast agents: they behave like small molecules in showing a rapid whole-body distribution (short distribution half-life), efficient renal clearance, and low accumulation in the nontarget organs. On the other hand, like conventional nanoparticles, they circulate in the blood (with a prolonged elimination half-life) and selectively accumulate in the tumor sites at high concentration for a long time through EPR effect. Not limited in fluorescence imaging, renal clearable NIR-emitting Au NPs (one example of molecular nanoprobes) can serves as CT contrast agent owing to large X-ray absorption of gold atoms,[50] and can also be easily converted into radiotracers for SPECT imaging when a little amount of radioactive ^{198}Au was incorporated into the Au cores during the synthesis.[93] A recent report of 2.8 nm ^{64}Cu-alloyed Au NPs provides a potential method to convert the renal clearable Au NPs to a PET imaging agent.[83] Therefore, among the nine strengths of small molecular probes and conventional nanoprobes for cancer imaging (listed at the beginning), the molecular nanoprobes meet the first eight advantages and the last one, the effect on the activity of labeled biomolecules, will be tested in future studies. Moreover, the integration of efficient renal clearance and the EPR effect results in a synergistic effect on cancer imaging. The tumor-to-liver ratios of renal clearable GS-AuNPs and PEG-AuNPs are one or two orders larger than those of nonrenal clearable AuNPs, while their tumor-to-kidney ratios are still comparable to some of nonrenal clearable NPs. A high tumor contrast index of 2.5 can be rapidly achieved by GS-AuNPs (~3 h p.i.) in fluorescence imaging, contributed form the rapid clearance of NPs from background tissue and their prolonged retention in the tumor.

To deliver the molecular nanoprobes into the clinical cancer diagnosis, many fundamental questions on the *in vivo* behaviors of renal clearable inorganic NPs still need to be addressed. For instance, (1) how intrinsic heterogeneity in the size distribution influences the renal excretion and tumor targeting of renal clearable inorganic NPs; (2) why renal clearable Au NPs showed stronger EPR effect than many other renal clearable NPs; (3) how to design better surface chemistries to enhance EPR effect without sacrificing renal clearance; (4) how the renal clearable inorganic NPs are filtrated through the kidneys; (5) while the effect of size, charge, shape, surface chemistry *etc*. on interaction between nanoparticles and biological systems has been investigated, these studies needs to be revisited when the particle size decreases down to the renal-clearable scale (HD < 6−8 nm); (6) synergistic integration of the EPR effect with active targeting strategy and environmentally responsive properties might lead to developing next generation of molecular nanoprobes; (7) small amount of large inorganic NPs such as 12 nm Au NPs (HD of 23 nm)[113] and silica NPs with core size of 33, 45 and 100−130 nm,[114−116] were also found in the urine; thus, unraveling renal clearance mechanism of these large NPs is also urgently needed; (8) in addition to *in vivo* behaviors, we still need to consider what imaging and therapeutic functionalities can be retained by inorganic NPs when the size decreases to renal clearable size range.

Moreover, as shown in the first clinical use of renal clearable inorganic NPs, the tumor area highlighted by ^{124}I-labeled cRGD-PEG-C dots on the PET image is very different from that obtained with [^{18}F]FDG.[109] This phenomenon suggests the two types of probes potentially light up different tumor structures, which reflect difference in pathological characteristics of tumor tissue because of their distinct tumor targeting mechanisms. The NPs can take advantage of the EPR effect (associated with angiogenesis), whereas [^{18}F]FDG relies on enhanced glucose metabolism of tumor cells. Combination of the two different tumor imaging strategies potentially generates new technologies for cancer diagnosis. Besides serving as contrast agents for cancer imaging, the renal clearable inorganic NPs with strong EPR effect have great potential in cancer therapy.[92,117−119] Either the NPs themselves show therapeutic efficacy or they can act as carrier for drug so as to improve the tumor targeting efficiency of drugs while reducing side effects caused by nonspecific accumulation of free drugs or large delivery systems in healthy organs. These molecular nanoparticles, with both imaging and therapeutic functionalities in a single formulation (theranostics),[120] open a possibility for delivery of nanomedicine into clinical cancer therapy. Although the enhanced and prolonged tumor accumulation of various nanoparticles is widely observed in preclinical animal studies, most nanoparticle-based drug delivery systems show limited improvements on the overall survival of patients compared with free drugs,[121] which demands continuing the efforts from experts from multiple disciplines to fundamentally understand clearance and tumor targeting of nanoparticles (e.g., imaging nanoprobes), so that they can eventually be translated into the clinical practices for healthcare improvement.

Conflict of Interest: The authors declare no competing financial interest.

Acknowledgment. The authors' work relevant to this review was supported by the NIH (R21EB009853 and 1R01DK103363), CPRIT (RP120588 and RP140544) and the start-up fund from the University of Texas at Dallas.

Supporting Information Available: Tables that summarize the renal clearance efficiencies of small molecular probes and the biodistribution and tumor targeting behaviors of renal clearable small molecular probes, conventional nonrenal clearable inorganic nanoprobes and renal clearable inorganic nanoprobes. The Supporting Information is available free of charge on the ACS Publications website at DOI: 10.1021/acsnano.5b01320.

REFERENCES AND NOTES

1. Weissleder, R.; Pittet, M. J. Imaging in the Era of Molecular Oncology. *Nature* **2008**, *452*, 580–589.
2. Frangioni, J. V. New Technologies for Human Cancer Imaging. *J. Clin. Oncol.* **2008**, *26*, 4012–4021.
3. Choi, H. S.; Liu, W.; Misra, P.; Tanaka, E.; Zimmer, J. P.; Ipe, B. I.; Bawendi, M. G.; Frangioni, J. V. Renal Clearance of Quantum Dots. *Nat. Biotechnol.* **2007**, *25*, 1165–1170.
4. Weissleder, R.; Kelly, K.; Sun, E. Y.; Shtatland, T.; Josephson, L. Cell-Specific Targeting of Nanoparticles by Multivalent Attachment of Small Molecules. *Nat. Biotechnol.* **2005**, *23*, 1418–1423.
5. Gao, X.; Cui, Y.; Levenson, R. M.; Chung, L. W.; Nie, S. *In Vivo* Cancer Targeting and Imaging with Semiconductor Quantum Dots. *Nat. Biotechnol.* **2004**, *22*, 969–976.
6. Rhyner, M. N.; Smith, A. M.; Gao, X. H.; Mao, H.; Yang, L. L.; Nie, S. M. Quantum Dots and Multifunctional Nanoparticles: New Contrast Agents for Tumor Imaging. *Nanomedicine* **2006**, *1*, 209–217.
7. Choi, H. S.; Liu, W.; Liu, F.; Nasr, K.; Misra, P.; Bawendi, M. G.; Frangioni, J. V. Design Considerations for Tumour-Targeted Nanoparticles. *Nat. Nanotechnol.* **2010**, *5*, 42–47.
8. Choi, H. S.; Frangioni, J. V. Nanoparticles for Biomedical Imaging: Fundamentals of Clinical Translation. *Mol. Imaging* **2010**, *9*, 291–310.
9. Kamaly, N.; Miller, A. D.; Bell, J. D. Chemistry of Tumour Targeted T-1 Based MRI Contrast Agents. *Curr. Top. Med. Chem.* **2010**, *10*, 1158–1183.
10. Prijic, S.; Sersa, G. Magnetic Nanoparticles as Targeted Delivery Systems in Oncology. *Radiol. Oncol.* **2011**, *45*, 1–16.
11. Boisselier, E.; Astruc, D. Gold Nanoparticles in Nanomedicine: Preparations, Imaging, Diagnostics, Therapies and Toxicity. *Chem. Soc. Rev.* **2009**, *38*, 1759–1782.
12. Lal, S.; Clare, S. E.; Halas, N. J. Nanoshell-Enabled Photothermal Cancer Therapy: Impending Clinical Impact. *Acc. Chem. Res.* **2008**, *41*, 1842–1851.
13. Jokerst, J. V.; Lobovkina, T.; Zare, R. N.; Gambhir, S. S. Nanoparticle Pegylation for Imaging and Therapy. *Nanomedicine* **2011**, *6*, 715–728.
14. Longmire, M.; Choyke, P. L.; Kobayashi, H. Clearance Properties of Nano-Sized Particles and Molecules as Imaging Agents: Considerations and Caveats. *Nanomedicine* **2008**, *3*, 703–717.
15. Harpur, E. S.; Worah, D.; Hals, P. A.; Holtz, E.; Furuhama, K.; Nomura, H. Preclinical Safety Assessment and Pharmacokinetics of Gadodiamide Injection, a New Magnetic

Resonance Imaging Contrast Agent. *Invest. Radiol.* **1993**, *28* (Suppl 1), S28–S43.
16. McLachlan, S. J.; Eaton, S.; Desimone, D. N. Pharmacokinetic Behavior of Gadoteridol Injection. *Invest. Radiol.* **1992**, *27*, S12–S15.
17. Bourin, M.; Jolliet, P.; Ballereau, F. An Overview of the Clinical Pharmacokinetics of X-Ray Contrast Media. *Clin. Pharmacokinet.* **1997**, *32*, 180–193.
18. Arnold, R. W.; Subramanian, G.; McAfee, J. G.; Blair, R. J.; Thomas, F. D. Comparison of ^{99m}Tc Complexes for Renal Imaging. *J. Nucl. Med.* **1975**, *16*, 357–367.
19. Taylor, A.; Eshima, D.; Fritzberg, A. R.; Christian, P. E.; Kasina, S. Comparison of Iodine-131 OIH and Technetium-99m MAG3 Renal Imaging in Volunteers. *J. Nucl. Med.* **1986**, *27*, 795–803.
20. Moran, J. K.; Lee, H. B.; Blaufox, M. D. Optimization of Urinary FDG Excretion During PET Imaging. *J. Nucl. Med.* **1999**, *40*, 1352–1357.
21. Choi, H. S.; Nasr, K.; Alyabyev, S.; Feith, D.; Lee, J. H.; Kim, S. H.; Ashitate, Y.; Hyun, H.; Patonay, G.; Strekowski, L.; et al. Synthesis and *In Vivo* Fate of Zwitterionic near-Infrared Fluorophores. *Angew. Chem., Int. Ed.* **2011**, *50*, 6258–6263.
22. Liu, J.; Yu, M.; Zhou, C.; Yang, S.; Ning, X.; Zheng, J. Passive Tumor Targeting of Renal-Clearable Luminescent Gold Nanoparticles: Long Tumor Retention and Fast Normal Tissue Clearance. *J. Am. Chem. Soc.* **2013**, *135*, 4978–4981.
23. Xie, H.; Wang, Z. J.; Bao, A.; Goins, B.; Phillips, W. T. *In Vivo* PET Imaging and Biodistribution of Radiolabeled Gold Nanoshells in Rats with Tumor Xenografts. *Int. J. Pharm.* **2010**, *395*, 324–330.
24. Liu, R. S.; Chou, T. K.; Chang, C. H.; Wu, C. Y.; Chang, C. W.; Chang, T. J.; Wang, S. J.; Lin, W. J.; Wang, H. E. Biodistribution, Pharmacokinetics and PET Imaging of [^{18}F]FMISO, [^{18}F]FDG and [^{18}F]FAc in a Sarcoma- and Inflammation-Bearing Mouse Model. *Nucl. Med. Biol.* **2009**, *36*, 305–312.
25. Andros, G.; Harper, P. V.; Lathrop, K. A.; McCardle, R. J. Pertechnetate-99m Localization in Man with Application to Thyroid Scanning and the Study of Thyroid Physiology. *J. Clin. Endocrinol. Metab.* **1965**, *25*, 1067–1076.
26. Zhao, Y.; Sultan, D.; Detering, L.; Cho, S.; Sun, G.; Pierce, R.; Wooley, K. L.; Liu, Y. Copper-64-Alloyed Gold Nanoparticles for Cancer Imaging: Improved Radiolabel Stability and Diagnostic Accuracy. *Angew. Chem., Int. Ed.* **2014**, *53*, 156–159.
27. Zhang, G.; Yang, Z.; Lu, W.; Zhang, R.; Huang, Q.; Tian, M.; Li, L.; Liang, D.; Li, C. Influence of Anchoring Ligands and Particle Size on the Colloidal Stability and *In Vivo* Biodistribution of Polyethylene Glycol-Coated Gold Nanoparticles in Tumor-Xenografted Mice. *Biomaterials* **2009**, *30*, 1928–1936.
28. Melancon, M. P.; Lu, W.; Yang, Z.; Zhang, R.; Cheng, Z.; Elliot, A. M.; Stafford, J.; Olson, T.; Zhang, J. Z.; Li, C. *In Vitro* and *In Vivo* Targeting of Hollow Gold Nanoshells Directed at Epidermal Growth Factor Receptor for Photothermal Ablation Therapy. *Mol. Cancer Ther.* **2008**, *7*, 1730–1739.
29. Cheng, K.; Kothapalli, S.-R.; Liu, H.; Koh, A. L.; Jokerst, J. V.; Jiang, H.; Yang, M.; Li, J.; Levi, J.; Wu, J. C.; et al. Construction and Validation of Nano Gold Tripods for Molecular Imaging of Living Subjects. *J. Am. Chem. Soc.* **2014**, *136*, 3560–3571.
30. Wang, Y.; Liu, Y.; Luehmann, H.; Xia, X.; Brown, P.; Jarreau, C.; Welch, M.; Xia, Y. Evaluating the Pharmacokinetics and *In Vivo* Cancer Targeting Capability of Au Nanocages by Positron Emission Tomography Imaging. *ACS Nano* **2012**, *6*, 5880–5888.
31. Piao, J.-G.; Wang, L.; Gao, F.; You, Y.-Z.; Xiong, Y.; Yang, L. Erythrocyte Membrane Is an Alternative Coating to Polyethylene Glycol for Prolonging the Circulation Lifetime of Gold Nanocages for Photothermal Therapy. *ACS Nano* **2014**, *8*, 10414–10425.
32. Hong, G. S.; Robinson, J. T.; Zhang, Y. J.; Diao, S.; Antaris, A. L.; Wang, Q. B.; Dai, H. J. *In Vivo* Fluorescence Imaging with Ag_2S Quantum Dots in the Second Near-Infrared Region. *Angew. Chem., Int. Ed.* **2012**, *51*, 9818–9821.
33. Sun, X.; Huang, X.; Guo, J.; Zhu, W.; Ding, Y.; Niu, G.; Wang, A.; Kiesewetter, D. O.; Wang, Z. L.; Sun, S.; et al. Self-Illuminating ^{64}Cu-Doped CdSe/ZnS Nanocrystals for *In Vivo* Tumor Imaging. *J. Am. Chem. Soc.* **2014**, *136*, 1706–1709.
34. Guo, W.; Sun, X.; Jacobson, O.; Yan, X.; Min, K.; Srivatsan, A.; Niu, G.; Kiesewetter, D. O.; Chang, J.; Chen, X. Intrinsically Radioactive [^{64}Cu]CuInS/ZnS Quantum Dots for PET and Optical Imaging: Improved Radiochemical Stability and Controllable Cerenkov Luminescence. *ACS Nano* **2015**, *9*, 488–495.
35. Gao, J.; Chen, K.; Xie, R.; Xie, J.; Lee, S.; Cheng, Z.; Peng, X.; Chen, X. Ultrasmall Near-Infrared Non-Cadmium Quantum Dots for *In Vivo* Tumor Imaging. *Small* **2010**, *6*, 256–261.
36. Gao, J.; Chen, K.; Xie, R.; Xie, J.; Yan, Y.; Cheng, Z.; Peng, X.; Chen, X. *In Vivo* Tumor-Targeted Fluorescence Imaging Using Near-Infrared Non-Cadmium Quantum Dots. *Bioconjugate Chem.* **2010**, *21*, 604–609.
37. Gao, J.; Chen, K.; Miao, Z.; Ren, G.; Chen, X.; Gambhir, S. S.; Cheng, Z. Affibody-Based Nanoprobes for HER2-Expressing Cell and Tumor Imaging. *Biomaterials* **2011**, *32*, 2141–2148.
38. Li, Z.; Wang, C.; Cheng, L.; Gong, H.; Yin, S.; Gong, Q.; Li, Y.; Liu, Z. PEG-Functionalized Iron Oxide Nanoclusters Loaded with Chlorin e6 for Targeted, NIR Light Induced, Photodynamic Therapy. *Biomaterials* **2013**, *34*, 9160–9170.
39. Song, X.; Gong, H.; Yin, S.; Cheng, L.; Wang, C.; Li, Z.; Li, Y.; Wang, X.; Liu, G.; Liu, Z. Ultra-Small Iron Oxide Doped Polypyrrole Nanoparticles for *In Vivo* Multimodal Imaging Guided Photothermal Therapy. *Adv. Funct. Mater.* **2014**, *24*, 1194–1201.
40. Crayton, S. H.; Tsourkas, A. pH-Titratable Superparamagnetic Iron Oxide for Improved Nanoparticle Accumulation in Acidic Tumor Microenvironments. *ACS Nano* **2011**, *5*, 9592–9601.
41. Park, J. H.; von Maltzahn, G.; Zhang, L.; Derfus, A. M.; Simberg, D.; Harris, T. J.; Ruoslahti, E.; Bhatia, S. N.; Sailor, M. J. Systematic Surface Engineering of Magnetic Nanoworms for *In Vivo* Tumor Targeting. *Small* **2009**, *5*, 694–700.
42. Liu, C.; Gao, Z.; Zeng, J.; Hou, Y.; Fang, F.; Li, Y.; Qiao, R.; Shen, L.; Lei, H.; Yang, W.; et al. Magnetic/Upconversion Fluorescent $NaGdF_4$:Yb,Er Nanoparticle-Based Dual-Modal Molecular Probes for Imaging Tiny Tumors *In Vivo*. *ACS Nano* **2013**, *7*, 7227–7240.
43. Jin, J.; Xu, Z.; Zhang, Y.; Gu, Y.-J.; Lam, M.H.-W.; Wong, W.-T. Upconversion Nanoparticles Conjugated with Gd^{3+}-Dota and RGD for Targeted Dual-Modality Imaging of Brain Tumor Xenografts. *Adv. Healthcare Mater.* **2013**, *2*, 1501–1512.
44. Lee, J.; Lee, T. S.; Ryu, J.; Hong, S.; Kang, M.; Im, K.; Kang, J. H.; Lim, S. M.; Park, S.; Song, R. RGD Peptide−Conjugated Multimodal $NaGdF_4$:Yb^{3+}/Er^{3+} Nanophosphors for Upconversion Luminescence, MR, and PET Imaging of Tumor Angiogenesis. *J. Nucl. Med.* **2013**, *54*, 96–103.
45. Wang, X.; Chen, J. T.; Zhu, H.; Chen, X.; Yan, X.-P. One-Step Solvothermal Synthesis of Targetable Optomagnetic Upconversion Nanoparticles for *In Vivo* Bimodal Imaging. *Anal. Chem.* **2013**, *85*, 10225–10231.
46. Chen, F.; Hong, H.; Zhang, Y.; Valdovinos, H. F.; Shi, S.; Kwon, G. S.; Theuer, C. P.; Barnhart, T. E.; Cai, W. *In Vivo* Tumor Targeting and Image-Guided Drug Delivery with Antibody-Conjugated, Radiolabeled Mesoporous Silica Nanoparticles. *ACS Nano* **2013**, *7*, 9027–9039.
47. Robinson, J. T.; Hong, G.; Liang, Y.; Zhang, B.; Yaghi, O. K.; Dai, H. *In Vivo* Fluorescence Imaging in the Second near-Infrared Window with Long Circulating Carbon Nanotubes Capable of Ultrahigh Tumor Uptake. *J. Am. Chem. Soc.* **2012**, *134*, 10664–10669.
48. Hong, H.; Yang, K.; Zhang, Y.; Engle, J. W.; Feng, L.; Yang, Y.; Nayak, T. R.; Goel, S.; Bean, J.; Theuer, C. P.; et al. *In Vivo*

Targeting and Imaging of Tumor Vasculature with Radiolabeled, Antibody-Conjugated Nanographene. *ACS Nano* **2012**, *6*, 2361–2370.
49. Benezra, M.; Penate-Medina, O.; Zanzonico, P. B.; Schaer, D.; Ow, H.; Burns, A.; DeStanchina, E.; Longo, V.; Herz, E.; Iyer, S.; et al. Multimodal Silica Nanoparticles Are Effective Cancer-Targeted Probes in a Model of Human Melanoma. *J. Clin. Invest.* **2011**, *121*, 2768–2780.
50. Zhou, C.; Long, M.; Qin, Y.; Sun, X.; Zheng, J. Luminescent Gold Nanoparticles with Efficient Renal Clearance. *Angew. Chem., Int. Ed.* **2011**, *50*, 3168–3172.
51. Liu, J.; Yu, M.; Ning, X.; Zhou, C.; Yang, S.; Zheng, J. Pegylation and Zwitterionization: Pros and Cons in the Renal Clearance and Tumor Targeting of Near-IR-Emitting Gold Nanoparticles. *Angew. Chem., Int. Ed.* **2013**, *52*, 12572–12576.
52. Alric, C.; Miladi, I.; Kryza, D.; Taleb, J.; Lux, F.; Bazzi, R.; Billotey, C.; Janier, M.; Perriat, P.; Roux, S.; et al. The Biodistribution of Gold Nanoparticles Designed for Renal Clearance. *Nanoscale* **2013**, *5*, 5930–5939.
53. Huang, X.; Zhang, F.; Zhu, L.; Choi, K. Y.; Guo, N.; Guo, J.; Tackett, K.; Anilkumar, P.; Liu, G.; Quan, Q.; et al. Effect of Injection Routes on the Biodistribution, Clearance, and Tumor Uptake of Carbon Dots. *ACS Nano* **2013**, *7*, 5684–5693.
54. Dreaden, E. C.; Alkilany, A. M.; Huang, X.; Murphy, C. J.; El-Sayed, M. A. The Golden Age: Gold Nanoparticles for Biomedicine. *Chem. Soc. Rev.* **2012**, *41*, 2740–2779.
55. Pérez-Juste, J.; Pastoriza-Santos, I.; Liz-Marzán, L. M.; Mulvaney, P. Gold Nanorods: Synthesis, Characterization and Applications. *Coord. Chem. Rev.* **2005**, *249*, 1870–1901.
56. Skrabalak, S. E.; Chen, J.; Sun, Y.; Lu, X.; Au, L.; Cobley, C. M.; Xia, Y. Gold Nanocages: Synthesis, Properties, and Applications. *Acc. Chem. Res.* **2008**, *41*, 1587–1595.
57. Lee, N.; Hyeon, T. Designed Synthesis of Uniformly Sized Iron Oxide Nanoparticles for Efficient Magnetic Resonance Imaging Contrast Agents. *Chem. Soc. Rev.* **2012**, *41*, 2575–2589.
58. Wang, F.; Liu, X. Recent Advances in the Chemistry of Lanthanide-Doped Upconversion Nanocrystals. *Chem. Soc. Rev.* **2009**, *38*, 976–989.
59. Zhou, J.; Liu, Z.; Li, F. Upconversion Nanophosphors for Small-Animal Imaging. *Chem. Soc. Rev.* **2012**, *41*, 1323–1349.
60. Vivero-Escoto, J. L.; Huxford-Phillips, R. C.; Lin, W. Silica-Based Nanoprobes for Biomedical Imaging and Theranostic Applications. *Chem. Soc. Rev.* **2012**, *41*, 2673–2685.
61. Li, Z.; Barnes, J. C.; Bosoy, A.; Stoddart, J. F.; Zink, J. I. Mesoporous Silica Nanoparticles in Biomedical Applications. *Chem. Soc. Rev.* **2012**, *41*, 2590–2605.
62. Cao, T.; Yang, Y.; Sun, Y.; Wu, Y.; Gao, Y.; Feng, W.; Li, F. Biodistribution of Sub-10 nm Peg-Modified Radioactive/Upconversion Nanoparticles. *Biomaterials* **2013**, *34*, 7127–7134.
63. Walkey, C. D.; Chan, W. C. W. Understanding and Controlling the Interaction of Nanomaterials with Proteins in a Physiological Environment. *Chem. Soc. Rev.* **2012**, *41*, 2780–2799.
64. Walkey, C. D.; Olsen, J. B.; Guo, H.; Emili, A.; Chan, W. C. W. Nanoparticle Size and Surface Chemistry Determine Serum Protein Adsorption and Macrophage Uptake. *J. Am. Chem. Soc.* **2012**, *134*, 2139–2147.
65. Yong, K.-T.; Roy, I.; Ding, H.; Bergey, E. J.; Prasad, P. N. Biocompatible Near-Infrared Quantum Dots as Ultrasensitive Probes for Long-Term *In Vivo* Imaging Applications. *Small* **2009**, *5*, 1997–2004.
66. Khlebtsov, N.; Dykman, L. Biodistribution and Toxicity of Engineered Gold Nanoparticles: A Review of *In Vitro* and *In Vivo* Studies. *Chem. Soc. Rev.* **2011**, *40*, 1647–1671.
67. Yong, K.-T.; Law, W.-C.; Hu, R.; Ye, L.; Liu, L.; Swihart, M. T.; Prasad, P. N. Nanotoxicity Assessment of Quantum Dots: From Cellular to Primate Studies. *Chem. Soc. Rev.* **2013**, *42*, 1236–1250.
68. Sadauskas, E.; Danscher, G.; Stoltenberg, M.; Vogel, U.; Larsen, A.; Wallin, H. Protracted Elimination of Gold Nanoparticles from Mouse Liver. *Nanomedicine* **2009**, *5*, 162–169.
69. Ye, L.; Yong, K.-T.; Liu, L.; Roy, I.; Hu, R.; Zhu, J.; Cai, H.; Law, W.-C.; Liu, J.; Wang, K.; et al. A Pilot Study in Non-Human Primates Shows No Adverse Response to Intravenous Injection of Quantum Dots. *Nat. Nanotechnol.* **2012**, *7*, 453–458.
70. Ballou, B.; Ernst, L. A.; Andreko, S.; Harper, T.; Fitzpatrick, J. A. J.; Waggoner, A. S.; Bruchez, M. P. Sentinel Lymph Node Imaging Using Quantum Dots in Mouse Tumor Models. *Bioconjugate Chem.* **2007**, *18*, 389–396.
71. Sun, Y.; Feng, W.; Yang, P.; Huang, C.; Li, F. The Biosafety of Lanthanide Upconversion Nanomaterials. *Chem. Soc. Rev.* **2015**, *44*, 1509–1525.
72. Kumar, R.; Roy, I.; Ohulchanskky, T. Y.; Vathy, L. A.; Bergey, E. J.; Sajjad, M.; Prasad, P. N. *In Vivo* Biodistribution and Clearance Studies Using Multimodal Organically Modified Silica Nanoparticles. *ACS Nano* **2010**, *4*, 699–708.
73. Gu, L.; Fang, R. H.; Sailor, M. J.; Park, J. H. *In Vivo* Clearance and Toxicity of Monodisperse Iron Oxide Nanocrystals. *ACS Nano* **2012**, *6*, 4947–4954.
74. Singh, R.; Pantarotto, D.; Lacerda, L.; Pastorin, G.; Klumpp, C.; Prato, M.; Bianco, A.; Kostarelos, K. Tissue Biodistribution and Blood Clearance Rates of Intravenously Administered Carbon Nanotube Radiotracers. *Proc. Natl. Acad. Sci. U. S. A.* **2006**, *103*, 3357–3362.
75. Hall, J. E. *Guyton and Hall Textbook of Medical Physiology*, 12th ed.; Saunders: Philadelphia. PA, 2011.
76. Burns, A. A.; Vider, J.; Ow, H.; Herz, E.; Penate-Medina, O.; Baumgart, M.; Larson, S. M.; Wiesner, U.; Bradbury, M. Fluorescent Silica Nanoparticles with Efficient Urinary Excretion for Nanomedicine. *Nano Lett.* **2009**, *9*, 442–448.
77. Zhou, Z.; Wang, L.; Chi, X.; Bao, J.; Yang, L.; Zhao, W.; Chen, Z.; Wang, X.; Chen, X.; Gao, J. Engineered Iron-Oxide-Based Nanoparticles as Enhanced T-1 Contrast Agents for Efficient Tumor Imaging. *ACS Nano* **2013**, *7*, 3287–3296.
78. Tang, S.; Chen, M.; Zheng, N. Sub-10-nm Pd Nanosheets with Renal Clearance for Efficient near-Infrared Photothermal Cancer Therapy. *Small* **2014**, *10*, 3139–3144.
79. Yang, S.; Sun, S.; Zhou, C.; Hao, G.; Liu, J.; Ramezani, S.; Yu, M.; Sun, X.; Zheng, J. Renal Clearance and Degradation of Glutathione-Coated Copper Nanoparticles. *Bioconjugate Chem.* **2015**, *26*, 511–519.
80. Park, J. H.; Gu, L.; von Maltzahn, G.; Ruoslahti, E.; Bhatia, S. N.; Sailor, M. J. Biodegradable Luminescent Porous Silicon Nanoparticles for *In Vivo* Applications. *Nat. Mater.* **2009**, *8*, 331–336.
81. Chou, L. Y. T.; Zagorovsky, K.; Chan, W. C. W. DNA Assembly of Nanoparticle Superstructures for Controlled Biological Delivery and Elimination. *Nat. Nanotechnol.* **2014**, *9*, 148–155.
82. Yang, K.; Wan, J.; Zhang, S.; Zhang, Y.; Lee, S.-T.; Liu, Z. *In Vivo* Pharmacokinetics, Long-Term Biodistribution, and Toxicology of Pegylated Graphene in Mice. *ACS Nano* **2011**, *5*, 516–522.
83. Zhao, Y.; Sultan, D.; Detering, L.; Luehmann, H.; Liu, Y. Facile Synthesis, Pharmacokinetic and Systemic Clearance Evaluation, and Positron Emission Tomography Cancer Imaging of ^{64}Cu-Au Alloy Nanoclusters. *Nanoscale* **2014**, *6*, 13501–13509.
84. Lynch, I.; Dawson, K. A. Protein-Nanoparticle Interactions. *Nano Today* **2008**, *3*, 40–47.
85. Zhou, C.; Long, M.; Qin, Y. P.; Sun, X. K.; Zheng, J. Luminescent Gold Nanoparticles with Efficient Renal Clearance. *Angew. Chem., Int. Ed.* **2011**, *50*, 3168–3172.
86. Meister, A.; Anderson, M. E. Glutathione. *Ann. Rev. Biochem.* **1983**, *52*, 711–760.
87. Rosi, N. L.; Giljohann, D. A.; Thaxton, C. S.; Lytton-Jean, A. K. R.; Han, M. S.; Mirkin, C. A. Oligonucleotide-Modified Gold Nanoparticles for Intracellular Gene Regulation. *Science* **2006**, *312*, 1027–1030.

88. Hong, R.; Han, G.; Fernandez, J. M.; Kim, B. J.; Forbes, N. S.; Rotello, V. M. Glutathione-Mediated Delivery and Release Using Monolayer Protected Nanoparticle Carriers. *J. Am. Chem. Soc.* **2006**, *128*, 1078–1079.
89. Yu, M.; Zhou, C.; Liu, J.; Hankins, J. D.; Zheng, J. Luminescent Gold Nanoparticles with pH-Dependent Membrane Adsorption. *J. Am. Chem. Soc.* **2011**, *133*, 11014–11017.
90. Semmler-Behnke, M.; Kreyling, W. G.; Lipka, J.; Fertsch, S.; Wenk, A.; Takenaka, S.; Schmid, G.; Brandau, W. Biodistribution of 1.4-and 18-nm Gold Particles in Rats. *Small* **2008**, *4*, 2108–2111.
91. Arvizo, R. R.; Miranda, O. R.; Moyano, D. F.; Walden, C. A.; Giri, K.; Bhattacharya, R.; Robertson, J. D.; Rotello, V. M.; Reid, J. M.; Mukherjee, P. Modulating Pharmacokinetics, Tumor Uptake and Biodistribution by Engineered Nanoparticles. *PLoS One* **2011**, *6*, e24374.
92. Zhang, C.; Li, C.; Liu, Y.; Zhang, J.; Bao, C.; Liang, S.; Wang, Q.; Yang, Y.; Fu, H.; Wang, K.; et al. Gold Nanoclusters-Based Nanoprobes for Simultaneous Fluorescence Imaging and Targeted Photodynamic Therapy with Superior Penetration and Retention Behavior in Tumors. *Adv. Funct. Mater.* **2015**, *25*, 1314–1325.
93. Zhou, C.; Hao, G. Y.; Thomas, P.; Liu, J. B.; Yu, M. X.; Sun, S. S.; Oz, O. K.; Sun, X. K.; Zheng, J. Near-Infrared Emitting Radioactive Gold Nanoparticles with Molecular Pharmacokinetics. *Angew. Chem., Int. Ed.* **2012**, *51*, 10118–10122.
94. Simpson, C. A.; Salleng, K. J.; Cliffel, D. E.; Feldheim, D. L. *In Vivo* Toxicity, Biodistribution, and Clearance of Glutathione-Coated Gold Nanoparticles. *Nanomedicine* **2013**, *9*, 257–263.
95. Chen, H.; Wang, G. D.; Tang, W.; Todd, T.; Zhen, Z.; Tsang, C.; Hekmatyar, K.; Cowger, T.; Hubbard, R. B.; Zhang, W.; et al. Gd-Encapsulated Carbonaceous Dots with Efficient Renal Clearance for Magnetic Resonance Imaging. *Adv. Mater.* **2014**, *26*, 6761–6766.
96. Li, S. D.; Huang, L. Pharmacokinetics and Biodistribution of Nanoparticles. *Mol. Pharmaceutics* **2008**, *5*, 496–504.
97. Perrault, S. D.; Walkey, C.; Jennings, T.; Fischer, H. C.; Chan, W. C. W. Mediating Tumor Targeting Efficiency of Nanoparticles through Design. *Nano Lett.* **2009**, *9*, 1909–1915.
98. Xing, H.; Zheng, X.; Ren, Q.; Bu, W.; Ge, W.; Xiao, Q.; Zhang, S.; Wei, C.; Qu, H.; Wang, Z.; et al. Computed Tomography Imaging-Guided Radiotherapy by Targeting Upconversion Nanocubes with Significant Imaging and Radiosensitization Enhancements. *Sci. Rep.* **2013**, *3*, 1751.
99. Liu, Z.; Cai, W.; He, L.; Nakayama, N.; Chen, K.; Sun, X.; Chen, X.; Dai, H. *In Vivo* Biodistribution and Highly Efficient Tumour Targeting of Carbon Nanotubes in Mice. *Nat. Nanotechnol.* **2007**, *2*, 47–52.
100. Matsumura, Y.; Maeda, H. A New Concept for Macromolecular Therapeutics in Cancer-Chemotherapy - Mechanism of Tumoritropic Accumulation of Proteins and the Antitumor Agent Smancs. *Cancer Res.* **1986**, *46*, 6387–6392.
101. Toy, R.; Bauer, L.; Hoimes, C.; Ghaghada, K. B.; Karathanasis, E. Targeted Nanotechnology for Cancer Imaging. *Adv. Drug Delivery Rev.* **2014**, *76*, 79–97.
102. Fang, J.; Nakamura, H.; Maeda, H. The EPR Effect: Unique Features of Tumor Blood Vessels for Drug Delivery, Factors involved, and Limitations and Augmentation of the Effect. *Adv. Drug Delivery Rev.* **2011**, *63*, 136–151.
103. Maeda, H. Tumor-Selective Delivery of Macromolecular Drugs *via* the EPR Effect: Background and Future Prospects. *Bioconjugate Chem.* **2010**, *21*, 797–802.
104. Wang, Y.; Liu, Y.; Luehmann, H.; Xia, X.; Wan, D.; Cutler, C.; Xia, Y. Radioluminescent Gold Nanocages with Controlled Radioactivity for Real-Time *In Vivo* Imaging. *Nano Lett.* **2013**, *13*, 581–585.
105. Wang, Y.; Black, K. C. L.; Luehmann, H.; Li, W.; Zhang, Y.; Cai, X.; Wan, D.; Liu, S.-Y.; Li, M.; Kim, P.; et al. Comparison Study of Gold Nanohexapods, Nanorods, and Nanocages for Photothermal Cancer Treatment. *ACS Nano* **2013**, *7*, 2068–2077.
106. Antaris, A. L.; Robinson, J. T.; Yaghi, O. K.; Hong, G.; Diao, S.; Luong, R.; Dai, H. Ultra-Low Doses of Chirality Sorted (6,5) Carbon Nanotubes for Simultaneous Tumor Imaging and Photothermal Therapy. *ACS Nano* **2013**, *7*, 3644–3652.
107. Liu, X.; Tao, H.; Yang, K.; Zhang, S.; Lee, S.-T.; Liu, Z. Optimization of Surface Chemistry on Single-Walled Carbon Nanotubes for *In Vivo* Photothermal Ablation of Tumors. *Biomaterials* **2011**, *32*, 144–151.
108. Sykes, E. A.; Chen, J.; Zheng, G.; Chan, W. C. W. Investigating the Impact of Nanoparticle Size on Active and Passive Tumor Targeting Efficiency. *ACS Nano* **2014**, *8*, 5696–5706.
109. Phillips, E.; Penate-Medina, O.; Zanzonico, P. B.; Carvajal, R. D.; Mohan, P.; Ye, Y. P.; Humm, J.; Gonen, M.; Kalaigian, H.; Schoder, H.; et al. Clinical Translation of an Ultrasmall Inorganic Optical-PET Imaging Nanoparticle Probe. *Sci. Transl. Med.* **2014**, *6*, 260ra149.
110. Jiang, T.; Olson, E. S.; Nguyen, Q. T.; Roy, M.; Jennings, P. A.; Tsien, R. Y. Tumor Imaging by Means of Proteolytic Activation of Cell-Penetrating Peptides. *Proc. Natl. Acad. Sci. U. S. A.* **2004**, *101*, 17867–17872.
111. Maeda, H.; Nakamura, H.; Fang, J. The Epr Effect for Macromolecular Drug Delivery to Solid Tumors: Improvement of Tumor Uptake, Lowering of Systemic Toxicity, and Distinct Tumor Imaging. *Adv. Drug Delivery Rev.* **2013**, *65*, 71–79.
112. Choi, H. S.; Gibbs, S. L.; Lee, J. H.; Kim, S. H.; Ashitate, Y.; Liu, F.; Hyun, H.; Park, G.; Xie, Y.; Bae, S.; et al. Targeted Zwitterionic near-Infrared Fluorophores for Improved Optical Imaging. *Nat. Biotechnol.* **2013**, *31*, 148–153.
113. Guerrero, S.; Herance, J. R.; Rojas, S.; Mena, J. F.; Gispert, J. D.; Acosta, G. A.; Albericio, F.; Kogan, M. J. Synthesis and *In Vivo* Evaluation of the Biodistribution of a ^{18}F-Labeled Conjugate Gold-Nanoparticle-Peptide with Potential Biomedical Application. *Bioconjugate Chem.* **2012**, *23*, 399–408.
114. Malfatti, M. A.; Palko, H. A.; Kuhn, E. A.; Turteltaub, K. W. Determining the Pharmacokinetics and Long-Term Biodistribution of SiO_2 Nanoparticles *In Vivo* Using Accelerator Mass Spectrometry. *Nano Lett.* **2012**, *12*, 5532–5538.
115. He, X.; Nie, H.; Wang, K.; Tan, W.; Wu, X.; Zhang, P. *In Vivo* Study of Biodistribution and Urinary Excretion of Surface-Modified Silica Nanoparticles. *Anal. Chem.* **2008**, *80*, 9597–9603.
116. Lu, J.; Liong, M.; Li, Z.; Zink, J. I.; Tamanoi, F. Biocompatibility, Biodistribution, and Drug-Delivery Efficiency of Mesoporous Silica Nanoparticles for Cancer Therapy in Animals. *Small* **2010**, *6*, 1794–1805.
117. Tang, S.; Chen, M.; Zheng, N. Multifunctional Ultrasmall Pd Nanosheets for Enhanced near-Infrared Photothermal Therapy and Chemotherapy of Cancer. *Nano Res.* **2015**, *8*, 165–174.
118. Zhang, X. D.; Luo, Z.; Chen, J.; Shen, X.; Song, S.; Sun, Y.; Fan, S.; Fan, F.; Leong, D. T.; Xie, J. Ultrasmall $Au_{10-12}(SG)_{10-12}$ Nanomolecules for High Tumor Specificity and Cancer Radiotherapy. *Adv. Mater.* **2014**, *26*, 4565–4568.
119. Zhang, X. D.; Luo, Z.; Chen, J.; Song, S.; Yuan, X.; Shen, X.; Wang, H.; Sun, Y.; Gao, K.; Zhang, L.; et al. Ultrasmall Glutathione-Protected Gold Nanoclusters as Next Generation Radiotherapy Sensitizers with High Tumor Uptake and High Renal Clearance. *Sci. Rep.* **2015**, *5*, 8669.
120. Lammers, T.; Aime, S.; Hennink, W. E.; Storm, G.; Kiessling, F. Theranostic Nanomedicine. *Acc. Chem. Res.* **2011**, *44*, 1029–1038.
121. Ernsting, M. J.; Murakami, M.; Roy, A.; Li, S. D. Factors Controlling the Pharmacokinetics, Biodistribution and Intratumoral Penetration of Nanoparticles. *J. Controlled Release* **2013**, *172*, 782–794.